


# nature physics



OCTOBER 2014 VOL 10 NO 10  
[www.nature.com/naturephysics](http://www.nature.com/naturephysics)

## Swimming by numbers

### **QUANTUM CONTROL**

Engineering with Zeno dynamics

### **SPECTROSCOPY**

Nonlinear inelastic electron scattering

### **INTERCONNECTED NETWORKS**

Naturally stable

Materials with a few weakly coupled layers can have a variety of complex structures, including twist angles, mismatched lattice periods or, as in the present case of rolled layers, different curvatures. It remains to be seen whether the coupling demonstrated by Liu and colleagues has consequences for other

properties of DWCNTs or other types of incommensurate layered systems.

João Lopes dos Santos is at Centro de Física do Porto and Departamento de Física e Astronomia, Faculdade de Ciências, Universidade do Porto, P4169-007 Porto, Portugal.  
e-mail: [jlsantos@fc.up.pt](mailto:jlsantos@fc.up.pt)

## References

1. Dean, C. R. *et al.* *Nature Nanotech.* **5**, 722–726 (2010).
2. Geim, A. K. & Grigorieva, I. V. *Nature* **499**, 419–425 (2013).
3. Uryu, S. & Ando, T. *Phys. Rev. B* **76**, 155434 (2007).
4. Liu, K. *et al.* *Nature Phys.* **10**, 737–742 (2014).
5. Liu, K. *et al.* *Nature Nanotech.* **7**, 325–329 (2012).

Published online: 7 September 2014

## FLUID DYNAMICS

# Swimming across scales

The myriad creatures that inhabit the waters of our planet all swim using different mechanisms. Now, a simple relation links key physical observables of underwater locomotion, on scales ranging from millimetres to tens of metres.

Johannes Baumgart and Benjamin M. Friedrich

**M**any animals swim by accelerating the liquid around them, using a regular undulatory motion powered by orchestrated muscle movements. But the movements of goldfish look vastly different from those of alligators, so the idea that they might be described by a universal mechanical principle seems optimistic — if not entirely unrealistic. Now, however, as they report in *Nature Physics*, Mattia Gazzola and colleagues<sup>1</sup> have found that common scaling relations characterize the swimming behaviours of a diverse set of marine creatures.

Gazzola *et al.*<sup>1</sup> used observational parameters, such as beat amplitude and frequency, to estimate physical quantities — including thrust, drag and pressure forces relevant for net propulsion. A measure of the thrust force is given by the mass of the fluid set in motion multiplied by its acceleration. The authors were able to describe the thrust generation of swimming organisms elegantly, using dimensionless numbers that characterize ratios of these quantities.

Dimensionless numbers have a long tradition of describing the scale-invariant features of fluid flow, providing key qualitative insight in fluid mechanics. For example, the so-called Reynolds number is defined as the ratio between two force scales: the relative magnitudes of inertial and viscous forces. Here, it is the typical speed of a swimmer, multiplied by a characteristic length scale and divided by the kinematic viscosity of the surrounding fluid.

The advantage of introducing such ratios is that any absolute force scale can be fully eliminated from the Navier–Stokes equations governing fluid flow, leaving only dimensionless parameters, and providing a reduced set of effective parameters. The form

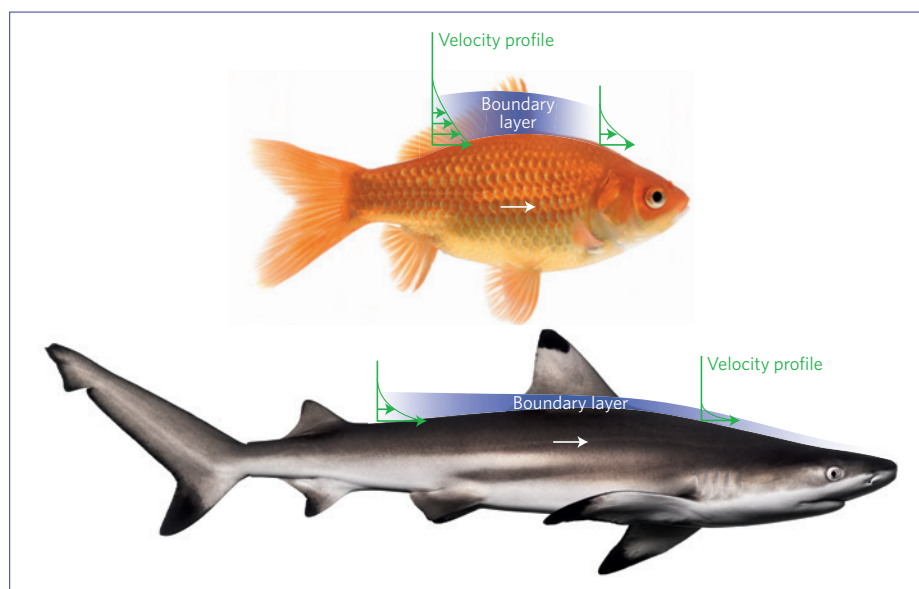


**Figure 1** | As a fish swims through viscous water, a layer of fluid is dragged along its body. This so-called boundary layer is proportionally thicker for small fish that experience lower Reynolds numbers compared with larger and fast-swimming fish. The fluid motion is illustrated by velocity profiles. Image of goldfish © David Cook/blueshiftstudios/Alamy; image of shark, © GlobalP/iStock/Thinkstock.

of the solution then depends only on these dimensionless parameters — one has to rescale it to yield a real-world solution. This is exploited in wind-tunnel experiments, for example, in which a scaled-down model is tested at the very same Reynolds number that applies to the real-world analogue. Length, force and time then have to be scaled appropriately.

The Reynolds number dictates the swimming experience. It is well known that swimming bacteria or sperm cells experience extremely low Reynolds numbers, implying that viscous forces dominate. If a sperm

flagellum were to stop beating all of a sudden, it would stop coasting within less than a millisecond — much like if you were to swim in honey. In this inertia-free world, scaling relations between the amplitude of swimming strokes and swimming speed have long been known. They are relatively easy to derive, as the corresponding mathematical equation governing viscous flow is linear, so solutions can simply be summed together.

At higher Reynolds numbers, applicable to the swimming of penguins and whales, convective effects dominate and new qualitative features emerge. Consider this

experiment: put a candle at a distance and try to extinguish it by either exhaling or inhaling. You'll find that reversing the sign of the boundary conditions does not simply reverse the flow — at large Reynolds numbers fluid dynamics is highly nonlinear and convective effects dominate. These flows are also prone to deterministic chaos, known in this context as turbulence.

These effects are all captured by the Navier–Stokes equations, which also describe the intricate flow patterns of whirling eddies, turbulent flows and the shock waves of transonic flights. Computing high-Reynolds-number flows is still very demanding, even on the fastest computers available. Although knowing the exact flow patterns in detail is an appealing idea, in the end one is quite often interested only in scalar quantities — in this case, the swimming speed of fish. Furthermore, in biology there is no need to squeeze out the last digit of precision, as is necessary, for example, in turbine design. Gazzola *et al.*<sup>1</sup> therefore took a promising approach by estimating the magnitude of such scalar quantities based on available experimental data.

The speed of swimming is determined by a balance of thrust and drag. Hydrodynamic friction arises from the relative motion of the fish skin with respect to the surrounding liquid. Specifically, the rate at which the fluid is sheared shows a characteristic decay as a function of distance from the swimmer, defining the boundary layer in which the viscous losses take place and kinetic energy is dissipated as heat<sup>2</sup>. This boundary layer becomes thinner, the faster the flow — a classic effect, well known to engineering students for the more simplified geometry of a flat plate. More than a century ago, Blasius investigated this type of problem<sup>3</sup>. He found self-similar solutions of the velocity profile, rescaled according to the Reynolds number. Gazzola *et al.*<sup>1</sup> applied this idea of

a viscous boundary layer to estimate the friction of a marine swimmer (Fig. 1), and its dependence on the swimmer's size, to derive a scaling exponent for the swimming speed. The theoretical prediction is indeed consistent with the biological data, as long as the amplitude of the undulatory body movements is smaller than the thickness of the boundary layer.

What happens for swimmers that are even faster? At such high Reynolds numbers, the viscous boundary layer is very thin and the deceleration of the fluid towards the body becomes important, resulting in a load through the conversion of kinetic energy into dynamic pressure, as known from Bernoulli's law. This effect is used by pilots, for example, when measuring their velocity with a pitot tube. Gazzola *et al.*<sup>1</sup> found a second scaling relation for this regime of high Reynolds numbers.

The authors' analysis showed that data from fish larvae, goldfish, alligators and whales can all be fitted with these two scaling laws, revealing a cross-over between viscous- and pressure-dominated regimes. An extensive set of two-dimensional simulations — treating the swimming creatures essentially as waving sheets — corroborates their findings. Two-dimensional calculations have a long tradition in fluid dynamics and have already been used<sup>4</sup> to understand self-propulsion at low Reynolds numbers. Strictly speaking, ignoring the third spatial dimension is a strong simplification. However, Gazzola *et al.*<sup>1</sup> compared selected three-dimensional simulations, some of them the largest ever conducted, to their two-dimensional results, and confirmed an analogous scaling relation.

What remains elusive is the transition point between the drag and pressure force regimes. It is an appealing idea that biology may have found ways to shift this point to low values and minimize the overall losses.

Indeed, at high Reynolds numbers, sharks are known to reduce drag through special patterning of their skin<sup>5</sup>.

The present work is an example of how physical laws — in this case, the physics of fluid flow — determine the operational range of biological mechanisms such as swimming. Physics sets effective constraints for biological evolution. The beauty of physical descriptions is that they often hold irrespective of a given length scale, and can thus describe phenomena occurring over a wide range of sizes. The absolute scale of lengths, times and forces can always be eliminated from a physical equation, leaving only dimensionless physical quantities. As these dimensionless quantities usually reflect biological design principles that are conserved across scales, universal scaling laws emerge.

It is interesting to compare this instance of physics constraining biological function to earlier work of allometric scaling laws, where it was argued that the hydrodynamics of blood flow in the transport networks of terrestrial animals define scaling relations that relate body size and metabolic activity<sup>6</sup>. The dawn of quantitative biology may yet reveal novel examples of such general scaling laws. □

Johannes Baumgart and Benjamin M. Friedrich are at the Max Planck Institute for the Physics of Complex Systems, 01187 Dresden, Germany. e-mail: [benjamin.friedrich@pks.mpg.de](mailto:benjamin.friedrich@pks.mpg.de)

## References

1. Gazzola, M., Argentina, M. & Mahadevan, L. *Nature Phys.* **10**, 758–761 (2014).
2. Schlichting, H. & Gersten K. *Boundary-Layer Theory* 8th edn (Springer, 2000).
3. Blasius, H. *Grenzschichten in Flüssigkeiten mit kleiner Reibung* [in German] PhD thesis, Univ. Göttingen (1907).
4. Taylor, G. *Proc. R. Soc. Lond. A* **211**, 225–239 (1952).
5. Reif, W.-E. & Dinkelacker, A. *Neues Jahrbuch für Geologie und Paläontologie, Abhandlungen* **164**, 184–187 (1982).
6. West, G. B., Brown, J. H. & Enquist, B. J. *Science* **276**, 122–126 (1997).

Published online: 14 September 2014

## MULTILAYER NETWORKS

# Dangerous liaisons?

Many networks interact with one another by forming multilayer networks, but these structures can lead to large cascading failures. The secret that guarantees the robustness of multilayer networks seems to be in their correlations.

Ginestra Bianconi

Natural complex systems evolve according to chance and necessity — trial and error — because they are driven by biological evolution. The expectation is that networks describing

natural complex systems, such as the brain and biological networks within the cell, should be robust to random failure. Otherwise, they would have not survived under evolutionary pressure. But many

natural networks do not live in isolation; instead they interact with one another to form multilayer networks — and evidence is mounting that random networks of networks are acutely susceptible to failure.

# Scaling macroscopic aquatic locomotion

Mattia Gazzola<sup>1</sup>, Médéric Argentina<sup>2,3</sup> and L. Mahadevan<sup>1,4\*</sup>

**Inertial aquatic swimmers that use undulatory gaits range in length  $L$  from a few millimetres to 30 metres, across a wide array of biological taxa. Using elementary hydrodynamic arguments, we uncover a unifying mechanistic principle characterizing their locomotion by deriving a scaling relation that links swimming speed  $U$  to body kinematics (tail beat amplitude  $A$  and frequency  $\omega$ ) and fluid properties (kinematic viscosity  $\nu$ ). This principle can be simply couched as the power law  $Re \sim Sw^\alpha$ , where  $Re = UL/\nu \gg 1$  and  $Sw = \omega AL/\nu$ , with  $\alpha = 4/3$  for laminar flows, and  $\alpha = 1$  for turbulent flows. Existing data from over 1,000 measurements on fish, amphibians, larvae, reptiles, mammals and birds, as well as direct numerical simulations are consistent with our scaling. We interpret our results as the consequence of the convergence of aquatic gaits to the performance limits imposed by hydrodynamics.**

Aquatic locomotion entails a complex interplay between the body of the swimmer and the induced flow in the environment<sup>1,2</sup>. It is driven by motor activity and controlled by sensory feedback in organisms ranging from bacteria to blue whales<sup>3</sup>. Locomotion at low Reynolds numbers ( $Re = UL/\nu \ll 1$ ) is governed by linear hydrodynamics and is consequently analytically tractable, whereas locomotion at high Reynolds numbers ( $Re \gg 1$ ) involves nonlinear inertial flows and is less well understood<sup>4</sup>. Although this is the regime that most macroscopic creatures larger than a few millimetres inhabit, as shown in Fig. 1a, the variety of sizes, morphologies and gaits makes it difficult to construct a unifying framework across taxa.

Thus, most studies have tried to take a more limited view by quantifying the problem of swimming in specific situations from experimental, theoretical and computational standpoints<sup>5–7</sup>. Beginning more than fifty years ago, experimental studies<sup>8–12</sup> started to quantify the basic kinematic properties associated with swimming in fish, while providing grist for later theoretical models. Perhaps the earliest and still most comprehensive of these studies was performed by Bainbridge<sup>8</sup>, who correlated size and frequency  $f = \omega/(2\pi)$  of several fish via the empirical linear relation  $U/L = (3/4)f - 1$ . However, he did not provide a mechanistic rationale based on fundamental physical principles.

The work of Bainbridge served as an impetus for a variety of theoretical models of swimming. The initial focus was on investigating thrust production associated with body motion at high Reynolds numbers, wherein inertial effects dominates viscous forces<sup>13,14</sup>. Later models also accounted for the elastic properties of the body and muscle activity<sup>15–18</sup>. The recent advent of numerical methods coupled with the availability of fast, cheap computational resources has triggered a new generation of direct numerical simulations to accurately resolve the full three-dimensional problem<sup>19–24</sup>. Although these provide detailed descriptions of the forces and flows during swimming, the large computational data sets associated with specific problems obscure the search for a broader perspective.

Inspired by the possibility of an evolutionary convergence of locomotory strategies ultimately limited by hydrodynamics, we bring together the specific and general perspectives associated with swimming using a combination of simple scaling arguments, detailed numerical simulations and a broad comparison with experiments. We start by recalling the basic physical mechanism underlying the inertial motion of a slender swimmer of length  $L$ , tail beat frequency  $\omega$  and amplitude  $A$ , moving at speed  $U$  (Fig. 1b) in a fluid of viscosity  $\mu$  and density  $\rho$  (kinematic viscosity  $\nu = \mu/\rho$ ). At high Reynolds numbers  $Re = UL/\nu \gg 1$ , inertial thrust is generated by the body-induced fluid acceleration, and balanced by the hydrodynamic resistance. We assume that the oscillation amplitude of motion is relatively small compared to the length of the organism, and that its body is slender. This implies that fluid acceleration can be effectively channelled into longitudinal thrust<sup>14</sup>. Furthermore, undulatory motions are considered to be in the plane, so that all quantities are characterized per unit depth.

In an incompressible, irrotational and inviscid flow the mass of fluid set into motion by the deforming body scales as  $\rho L^2$  per unit depth<sup>25</sup>, assuming that the wavelength associated with the undulatory motions scales with the body length  $L$ , consistent with experimental and empirical observations. The acceleration of the surrounding fluid scales as  $A\omega^2$  (Fig. 1c) and therefore the reaction force exerted by the fluid on the swimmer scales as  $\rho L^2 A\omega^2$ . As the body makes a local angle with the direction of motion that scales as  $A/L$ , this leads to the effective thrust  $\rho\omega^2 A^2 L$ , as shown in Fig. 1c.

The viscous resistance to motion (skin drag) per unit depth scales as  $\mu UL/\delta$ , where  $\delta$  is the thickness of the boundary layer<sup>26</sup>. For fast laminar flows the classical Blasius theory shows  $\delta \sim LRe^{-1/2}$ , so that the skin drag force due to viscous shear scales as  $\rho(\nu L)^{1/2} U^{3/2}$ , as shown in Fig. 1c. Balancing thrust and skin drag yields the relation  $U \sim A^{4/3} \omega^{4/3} L^{1/3} \nu^{-1/3}$  which we may rewrite as

$$Re \sim Sw^{4/3} \quad (1)$$

where  $Sw = \omega AL/\nu$  is the dimensionless swimming number, which can be understood as a transverse Reynolds number characterizing the undulatory motions that drive swimming. This simple scaling relationship links the locomotory input variables that describe the gait of the swimmer  $A, \omega$  via the swimming number  $Sw$  to the locomotory output velocity  $U$  via the longitudinal Reynolds number  $Re$ .

At very high Reynolds numbers ( $Re > 10^3 - 10^4$ ), the boundary layer around the body becomes turbulent and the pressure drag dominates the skin drag<sup>26</sup>. The corresponding force scales as  $\rho U^2 L$  per unit depth, which when balanced by the thrust yields

$$Re \sim Sw \quad (2)$$

<sup>1</sup>School of Engineering and Applied Sciences, Harvard University, Cambridge, Massachusetts 02138, USA, <sup>2</sup>Université Nice Sophia-Antipolis, Institut non linéaire de Nice, CNRS UMR 7335, 1361 route des Lucioles, 06560 Valbonne, France, <sup>3</sup>Institut Universitaire de France, 103, boulevard Saint-Michel, 75005 Paris, France, <sup>4</sup>Department of Organismic and Evolutionary Biology, Department of Physics, Wyss Institute for Biologically Inspired Engineering, Kavli Institute for Nanobio Science and Technology, Harvard University, Cambridge, Massachusetts 02138, USA. \*e-mail: [lm@seas.harvard.edu](mailto:lm@seas.harvard.edu)

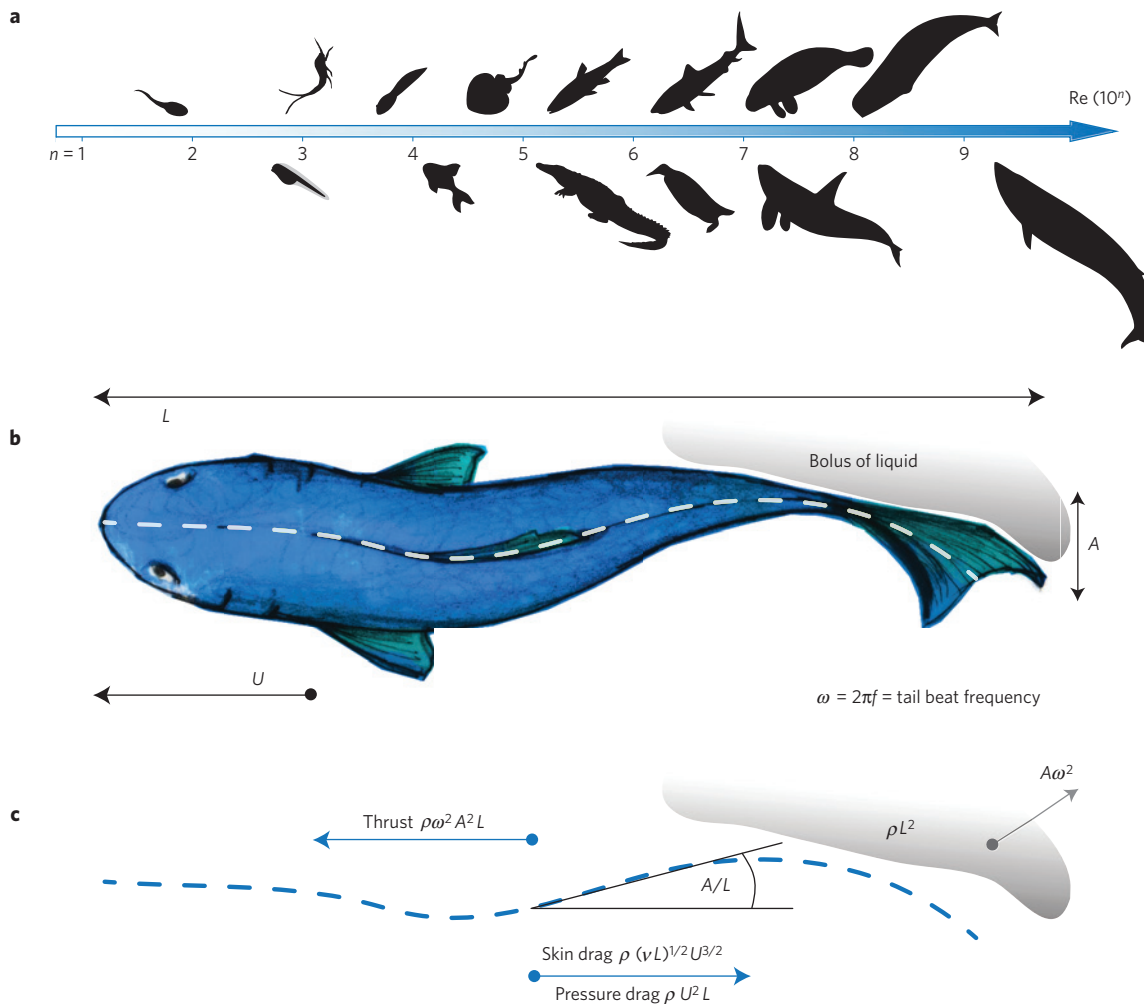


**Figure 1 | Aquatic swimming.** **a**, The organisms considered here (Supplementary Information) span eight orders of magnitude in Reynolds number and encompass larvae (from mayfly to zebrafish), fish (from goldfish, to stingrays and sharks), amphibians (tadpoles), reptiles (alligators), marine birds (penguins) and large mammals (from manatees and dolphins to belugas and blue whales). Blue fish sketch by Margherita Gazzola. **b**, Swimmer of length  $L$  is propelled forward with velocity  $U$  by pushing a bolus of water<sup>14,20,24</sup> through body undulations characterized by tail beat amplitude  $A$  and frequency  $\omega$ . **c**, Thrust and drag forces on a swimmer. Thrust is the reaction force associated with accelerating ( $A\omega^2$ ) the mass of liquid per unit depth  $\rho L^2$  weighted by the local angle  $A/L$  (therefore  $\rho LA$  may be understood as the mass of liquid channelled downstream). For laminar boundary layers, the drag is dominated by viscous shear (skin drag), whereas for turbulent boundary layers, the drag is dominated by pressure (pressure drag).

As most species when swimming at high speeds maintain an approximately constant value of the specific tail beat amplitude  $A/L$  (refs 8,11), relation (2) reduces to  $U/L \sim f$ , providing a mechanistic basis for Bainbridge's empirical relation.

In Fig. 2a, we plot all data from over 1,000 different measurements compiled from a variety of sources (Supplementary Information) in terms of  $Re$  and  $Sw$ , for fish (from zebrafish larvae to stingrays and sharks), amphibians (tadpoles), reptiles (alligators), marine birds (penguins) and large mammals (from manatees and dolphins to belugas and blue whales). The organisms varied in size from 0.001 to 30 m, while their propulsion frequency varied from 0.25 to 100 Hz. The dimensionless numbers we use to scale the data provides a natural division of aquatic organisms by size, with fish larvae at the bottom left, followed by small amphibians, fish, birds, reptiles, and large marine mammals at the top right. We see that the data, which span nearly eight orders of magnitude in the Reynolds number, are in agreement with our predictions, and show a natural crossover from the laminar power law (1) to the turbulent power law (2) at a Reynolds number of approximately  $Re \simeq 3,000$ . To understand this, we note that the skin friction starts to be dominated by the pressure drag when

the thickness of the laminar boundary layer is comparable to half the oscillation amplitude. Therefore, a minimal estimate for the critical Reynolds number  $Re_{\text{critical}}$  associated with the laminar-turbulent transition is given by the relation  $\delta \simeq A/2$ . For a flat plate<sup>26</sup>  $\delta = 5\sqrt{\nu L/U}$  and given a typical value of  $A/L = 0.2$ , we obtain  $Re_{\text{critical}} \simeq (10L/A)^2 = 2,500$ , which is in agreement with experimental data.

Naturally, some organisms do not hew exactly to our scaling relationships. Indeed, sirenians (manatees) slightly fall below the line, whereas anuran tadpoles lie slightly above it (Supplementary Information). We ascribe these differences to intermittent modes of locomotion involving a combination of acceleration, steady swimming and coasting that these species often use. Other reasons for the deviations could be related to different gaits in which part or the entire body is used, as in carangiform or anguilliform motion. Moreover, morphological variations associated with the body, tail and fins may play a role by directly affecting the hydrodynamic profile, or indirectly by modifying the gaits. However, the agreement with our minimal scaling arguments suggests that the role of these specifics is secondary, given the variety of shapes and gaits encompassed in our experimental data set.

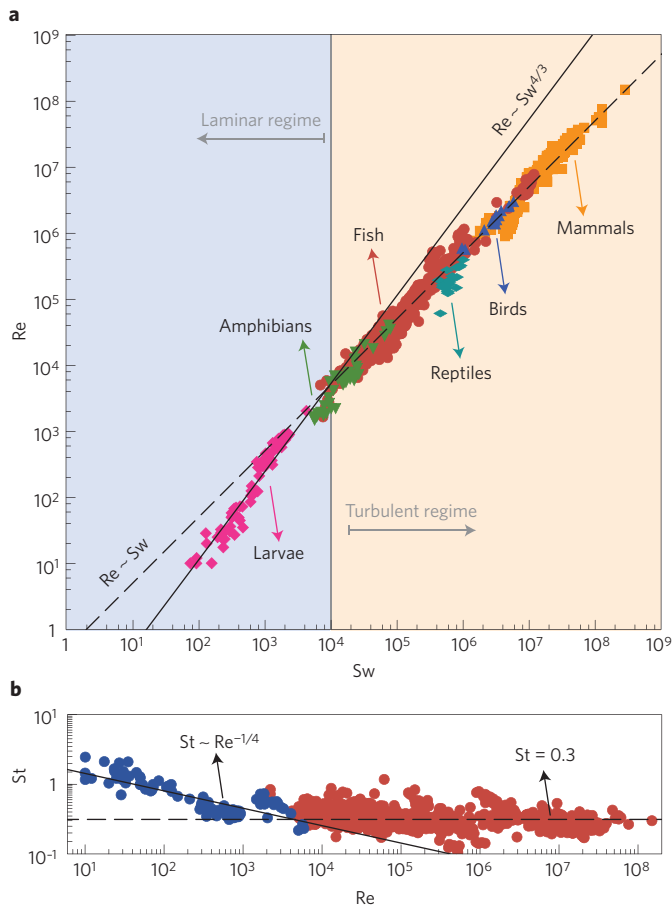


**Figure 2 | Scaling aquatic locomotion: measurements.** **a**, Data from amphibians, larvae, fish, marine birds and mammals show that the scaled speed of the organism  $Re = UL/\nu$  varies with the scaled frequency of the oscillatory propulsor  $Sw = \omega AL/\nu$  according to equations (1) and (2) over eight decades. Data fit for the laminar regime yields  $Re = 0.03Sw^{1.31}$  with  $R^2 = 0.95$ , and for the turbulent regime yields  $Re = 0.4Sw^{1.02}$  with  $R^2 = 0.99$ . **b**, The Strouhal number  $St = fA/U$ , with  $f = \omega/2\pi$ , depends weakly on Reynolds number  $St \sim Re^{-1/4}$  for  $Sw < 10^4$  (blue) and is independent for  $Sw > 10^4$  (red), consistent with our scaling relationships and earlier observations<sup>30</sup>.

Because aquatic organisms live in water, testing the dependence of our scaling relationships on viscosity requires manipulating the environment. Although this has been done on occasion<sup>27</sup> and is consistent with our scaling relations (Supplementary Information), numerical simulations of the Navier–Stokes equations coupled to the motion of a swimming body allow us to test our power laws directly by varying  $Sw$  via the viscosity  $\nu$  only (Supplementary Information). In Fig. 3, we show the results for two-dimensional anguilliform swimmers<sup>28,29</sup>. The data from our numerical experiments straddle both sides of the crossover from the laminar to the turbulent regime and are in quantitative agreement with our minimal scaling theory, and our simple estimate for  $Re_{critical}$ . To further challenge our theoretical scaling relationships, in Fig. 3, we plot the results of three-dimensional simulations performed by various groups using different numerical techniques<sup>19,22,24,28</sup>; they also collapse onto the same power laws (details in Supplementary Information). The agreement with both two- and three-dimensional numerical simulations, which are not affected by environmental and behavioural vagaries, gives us further confidence in our theory.

Traditionally, most studies of locomotion use the Strouhal number  $St = \omega A/U$ , a variable borrowed from engineering, to

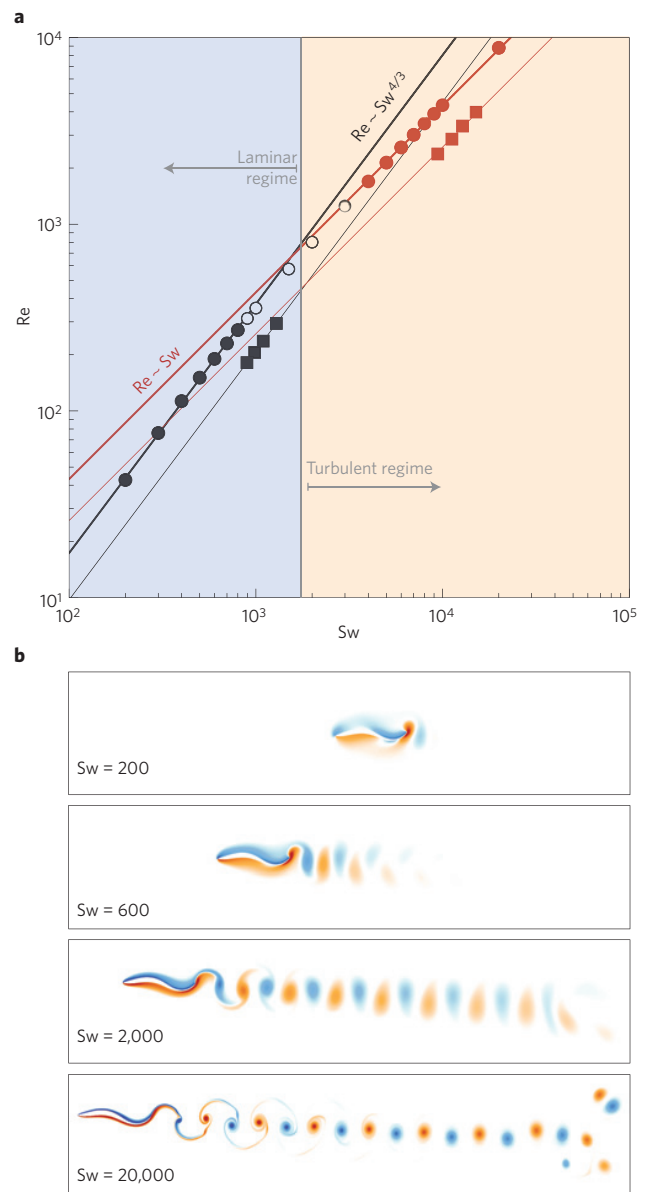


**Figure 3 | Scaling aquatic locomotion: simulations.** **a**, Two- and three-dimensional direct numerical simulations of swimming creatures confirm equations (1) and (2). Circles correspond to two-dimensional simulations, while squares correspond to three-dimensional simulations (details about sources and numerical techniques can be found in the Supplementary Information). In the case of two-dimensional simulations, a data fit for the laminar regime yields  $Re = 0.04Sw^{4/3}$  with  $R^2 = 0.99$ , and for the turbulent regime yields  $Re = 0.43Sw$  with  $R^2 = 0.99$ . Remarkably, three-dimensional simulations performed by various groups<sup>19,22,24,28</sup> and with different numerical techniques (Supplementary Information) confirm our scaling relations ( $Re = 0.02Sw^{4/3}$  with  $R^2 = 1.00$ , and  $Re = 0.26Sw$  with  $R^2 = 0.99$ ). **b**, For several  $Sw$  we display the vorticity fields (red—positive, blue—negative) generated by a two-dimensional anguilliform swimmer initially located on the rightmost side of the figure.

characterize the underlying dynamics. Although this is reasonable for many engineering applications such as vortex shedding, vibration and so on, in a biological context it is worth emphasizing that  $St$  confounds input  $A-\omega$  and output  $U$  variables, captures only one length scale by assuming  $A \sim L$ , and does not account for varying fluid environments characterized by  $\nu$ . For biological locomotion,  $Sw$  is a more natural variable as it captures the

two length scales associated with the tail amplitude and the body size, accounts for the fluid environment, and allows us to seamlessly relate the input kinematics  $A-\omega$  to the output velocity  $U$ . Nevertheless, writing equations (1) and (2) in terms of  $St$  yields  $Sw = Re \cdot St$ ; therefore  $St \sim Re^{-1/4}$ , for laminar flows, and  $St = \text{const}$ , for turbulent flows, showing little or no influence of the Reynolds number on the Strouhal number. This direct consequence of our theory is consistent with experimental observations (Fig. 2b) and provides a physical basis for the findings<sup>30</sup> that most swimming and flying animals operate in a relatively narrow range of  $St$ .

Despite the vast phylogenetic spread of inertial swimmers (Supplementary Information), we find that their locomotory dynamics is governed by the elementary hydrodynamical principles embodied in the power law  $Re \sim Sw^\alpha$ , with  $\alpha = 4/3$  for laminar regimes and  $\alpha = 1$  for turbulent boundary layers. This scaling relation follows by characterizing the biological diversity of aquatic locomotion in terms of the physical constraints of inertial swimming, a convergent evolutionary strategy for moving through water in macroscopic creatures. Recalling that the phase space  $Sw-Re$  relates the input transverse Reynolds number  $Sw$  to the output longitudinal Reynolds number  $Re$ , our scaling relations might also be interpreted as the edge of optimal steady locomotor performance in this space, separating the inefficient (below) from the unattainable (above) steady regimes in oscillatory aquatic propulsive systems. We anticipate that if general principles for aerial or terrestrial locomotion exist, they may well be found by considering the physical limits dictated by their respective environments.

Received 10 April 2014; accepted 28 July 2014;  
published online 14 September 2014

## References

- Pedley, T. J. *Scale Effects in Animal Locomotion* (Cambridge Univ. Press, 1977).
- Vogel, S. *Life in Moving Fluids: The Physical Biology of Flow* (Princeton Univ. Press, 1996).
- Fish, F. E. & Lauder, G. V. Passive and active flow control by swimming fishes and mammals. *Annu. Rev. Fluid Mech.* **38**, 193–224 (2006).
- Childress, S. *Mechanics of Swimming and Flying* (Cambridge Univ. Press, 1981).
- Hertel, H. *Structure, Form, Movement* (Reinhold, 1966).
- Triantafyllou, M. S., Triantafyllou, G. S. & Yue, D. K. P. Hydrodynamics of fishlike swimming. *Annu. Rev. Fluid Mech.* **32**, 33–53 (2000).
- Wu, T. Y. Fish swimming and bird/insect flight. *Annu. Rev. Fluid Mech.* **43**, 25–58 (2011).
- Bainbridge, R. The speed of swimming of fish as related to size and to the frequency and amplitude of the tail beat. *J. Exp. Biol.* **35**, 109–133 (1958).
- Webb, P. W., Kostecki, P. T. & Stevens, E. D. The effect of size and swimming speed on locomotor kinematics of rainbow trout. *J. Exp. Biol.* **109**, 77–95 (1984).
- Videler, J. J. & Wardle, C. S. Fish swimming stride by stride: speed limits and endurance. *Rev. Fish Biol. Fisheries* **1**, 23–40 (1991).
- Mchenry, M., Pell, C. & Long, J. H. Jr Mechanical control of swimming speed: Stiffness and axial wave form in undulating fish models. *J. Exp. Biol.* **198**, 2293–305 (1995).
- Long, J. H. Jr Muscles, elastic energy, and the dynamics of body stiffness in swimming eels. *Am. Zool.* **38**, 771–792 (1998).
- Taylor, G. I. Analysis of the swimming of long and narrow animals. *Proc. R. Soc. Lond. A* **214**, 158–183 (1952).
- Lighthill, M. J. Large-amplitude elongated-body theory of fish locomotion. *Proc. R. Soc. Lond. B* **179**, 125–138 (1971).
- Hess, F. & Videler, J. J. Fast continuous swimming of saithe (*Pollachius virens*): A dynamic analysis of bending moments and muscle power. *J. Exp. Biol.* **109**, 229–251 (1984).
- Cheng, J. Y., Pedley, T. J. & Altringham, J. D. A continuous dynamic beam model for swimming fish. *Phil. Trans. R. Soc. Lond. B* **353**, 981–997 (1998).
- McMillen, T., Williams, T. & Holmes, P. Nonlinear muscles, passive viscoelasticity and body taper conspire to create neuromechanical phase lags in anguilliform swimmers. *PLoS Comput. Biol.* **4**, e1000157 (2008).
- Alben, S., Witt, C., Baker, T. V., Anderson, E. & Lauder, G. V. Dynamics of freely swimming flexible foils. *Phys. Fluids* **24**, 051901 (2012).
- Kern, S. & Koumoutsakos, P. Simulations of optimized anguilliform swimming. *J. Exp. Biol.* **209**, 4841–4857 (2006).
- Gazzola, M., van Rees, W. M. & Koumoutsakos, P. C-start: Optimal start of larval fish. *J. Fluid Mech.* **698**, 5–18 (2012).
- Tytell, E. D., Hsu, C. Y., Williams, T. L., Cohen, A. H. & Fauci, L. J. Interactions between internal forces, body stiffness, and fluid environment in a neuromechanical model of lamprey swimming. *Proc. Natl Acad. Sci. USA* **107**, 19832–19837 (2010).
- Tytell, E. D. *et al.* Disentangling the functional roles of morphology and motion in the swimming of fish. *Integr. Comp. Biol.* **50**, 1140–1154 (2010).
- Bhalla, A. P. S., Griffith, B. E. & Patankar, N. A. A forced damped oscillation framework for undulatory swimming provides new insights into how propulsion arises in active and passive swimming. *PLoS Comput. Biol.* **9**, e1003097 (2013).
- van Rees, W. M., Gazzola, M. & Koumoutsakos, P. Optimal shapes for anguilliform swimmers at intermediate Reynolds numbers. *J. Fluid Mech.* **722**, R3 (2013).
- Batchelor, G. K. *An Introduction to Fluid Dynamics* (Cambridge Univ. Press, 1967).
- Landau, L. D. & Lifshitz, E. M. *Fluid Mechanics* (Pergamon Press, 1959).
- Horner, A. M. & Jayne, B. C. The effects of viscosity on the axial motor pattern and kinematics of the African lungfish (*Protopterus annectens*) during lateral undulatory swimming. *J. Exp. Biol.* **211**, 1612–1622 (2008).
- Gazzola, M., Chatelain, P., van Rees, W. M. & Koumoutsakos, P. Simulations of single and multiple swimmers with non-divergence free deforming geometries. *J. Comput. Phys.* **230**, 7093–7114 (2011).
- Gazzola, M., Hejazialhosseini, B. & Koumoutsakos, P. Reinforcement learning and wavelet adapted vortex methods for simulations of self-propelled swimmers. *SIAM J. Sci. Comput.* **36**, B622–B639 (2014).
- Taylor, G. K., Nudds, R. L. & Thomas, A. L. R. Flying and swimming animals cruise at a Strouhal number tuned for high power efficiency. *Nature* **425**, 707–711 (2003).

## Acknowledgements

We thank the Swiss National Science Foundation, and the MacArthur Foundation for partial financial support. We also thank W. van Rees, B. Hejazialhosseini and P. Koumoutsakos of the CSElab at ETH Zurich for their help with the computational aspects of the study, and Margherita Gazzola for her sketches.

## Author contributions

M.G., M.A. and L.M. conceived the study, developed the theory, collected and analysed the experimental data and wrote the paper. M.G. performed the 2D numerical simulations.

## Additional information

Supplementary information is available in the [online version of the paper](http://www.nature.com/naturephysics). Reprints and permissions information is available online at [www.nature.com/reprints](http://www.nature.com/reprints). Correspondence and requests for materials should be addressed to L.M.

## Competing financial interests

The authors declare no competing financial interests.

# Scaling macroscopic aquatic locomotion

Mattia Gazzola\*, Médéric Argentina<sup>†‡</sup>, and L. Mahadevan\*

\*Department of Physics and School of Engineering and Applied Sciences, Harvard University, Cambridge, MA 02138, USA [mgazzola@seas.harvard.edu](mailto:mgazzola@seas.harvard.edu), [lm@seas.harvard.edu](mailto:lm@seas.harvard.edu)

<sup>†</sup> Université Nice Sophia-Antipolis, Institut non linéaire de Nice, CNRS UMR 7335, 1361 route des lucioles, 06560 Valbonne, France

<sup>‡</sup> Institut Universitaire de France, 103, boulevard Saint-Michel, 75005 Paris, France  
[mederic.argentina@unice.fr](mailto:mederic.argentina@unice.fr)

Correspondence to: [lm@seas.harvard.edu](mailto:lm@seas.harvard.edu)

## Material and methods

### 1 Simulations of swimmers in fluids of varying viscosity

To validate our scaling laws, we performed two-dimensional direct numerical simulations of self-propelled swimmers immersed in a viscous flow. We systematically scanned the swimming number  $Sw$  over two orders of magnitude in the range  $2 \cdot 10^2 < Sw < 2 \cdot 10^4$  that straddles the cross-over regime from laminar to turbulent flows to determine its impact on the resulting Reynolds number.

Numerical simulations are particularly useful in the context of this work as, unlike experimental observations, they are not affected by environmental and behavioral vagaries and allow us to vary the swimming number  $Sw = \omega AL/\nu$  by modifying the environment through  $\nu$ , instead of using the swimmers' kinematic properties  $\omega$ ,  $A$ , and  $L$ . This crucially tests the dependence of our scaling laws on the kinematic viscosity  $\nu$ .

Simulations are performed via a state-of-the-art numerical scheme based on multiresolution remeshed vortex methods coupled with Brinkman penalization and projection approach [31–34], to combine computational efficiency and physical accuracy. These techniques have been extensively validated on several benchmark problems involving flow past bluff bodies, sedimentation of dense objects, and self-propelled swimming [32]. Furthermore, it has been verified against experimental observations of larval zebrafish fast starts [35, 36] and applied to a number of engineering and biological problems [37, 36, 38].

Here we briefly review the employed methodology and present the results in the light of the theory proposed in this work.

**Flow conditions** The swimmers were characterized by a swimming number  $Sw$  spanning the range  $2 \cdot 10^2 < Sw < 2 \cdot 10^4$ , typical of larvae and small fish (2 – 3cm). The swimming number  $Sw = \omega AL/\nu$  is varied by modifying only the flow kinematic viscosity  $\nu$ , while maintaining the kinematic parameters  $\omega$ ,  $A$ ,  $L$  constant.

**Midline kinematics** The midline kinematics of the swimmers considered here are fixed and identical in all simulations. We employed the motion pattern proposed by Carling [39], representative of anguilliform swimming. This choice is motivated by the fact that larval zebrafish exhibit anguilliform motion [40]. The swimming pattern defined by Carling is characterized by a normalized tail beat amplitude  $\lambda = A/L = 0.25$ . The tail beat frequency is set to  $\omega = 2\pi$  (period  $T = 1$ ) throughout the present work.

**Shape** The two-dimensional geometry of the swimmers is fixed and identical for all simulations and is determined via the parameterization proposed in [38]. The width profile of the fish is described by a cubic B-splines ( $N = 6$  control points  $\beta_i$  with  $i = 0, \dots, N - 1$ ) function of the axial coordinate  $0 \leq s \leq L$ . The first and last control points are set to  $(s_0, \beta_0) = (0, 0)$  and  $(s_{N-1}, \beta_{N-1}) = (L, 0)$  to maintain  $C^1$  continuity at the extrema. The remaining control points, uniformly distributed along the length of the swimmer, are set to  $\beta_1 = 1.4e^{-2}$   $\beta_2 = 4.6e^{-2}$   $\beta_3 = 2.2e^{-3}$   $\beta_4 = 5.8e^{-3}$ . These settings are characteristic of a streamlined fast swimmer [38].

**Numerical method** We consider two-dimensional simulations of a self-propelled swimmer immersed in a viscous flow in the infinite domain  $\Sigma$ . The system is governed by the incompressible Navier-Stokes equations:

$$\nabla \cdot \mathbf{u} = 0, \quad \frac{\partial \mathbf{u}}{\partial t} + (\mathbf{u} \cdot \nabla) \mathbf{u} = -\frac{1}{\rho} \nabla p + \nu \nabla^2 \mathbf{u}, \quad \mathbf{x} \in \Sigma \setminus \Omega \quad (1)$$

where  $\Omega$  is the volume occupied by the swimmer. The no-slip boundary condition at the geometrical interface  $\partial\Omega$  enforces the fluid velocity  $\mathbf{u}$  to match the local swimming velocity  $\mathbf{u}_s$ . The feedback from the flow to the body is governed by the equations of motion:

$$m_s \ddot{\mathbf{x}}_s = \mathbf{F}^H, \quad d(\mathbf{I}_s \dot{\boldsymbol{\theta}}_s)/dt = \mathbf{M}^H, \quad (2)$$

where  $\mathbf{F}^H$  and  $\mathbf{M}^H$  are the hydrodynamic force and momentum exerted by the fluid on the body, which is characterized by its centre of mass  $\mathbf{x}_s$ , angular velocity  $\dot{\boldsymbol{\theta}}_s$ , mass  $m_s$  and moment of inertia  $\mathbf{I}_s$ .

The numerical method to integrate the system (1-2) consists of a remeshed vortex method, coupled with a Brinkman penalization technique to approximate the no-slip boundary condition and a projection method [31, 32], to capture the action from the fluid to the body. The body geometry is defined by the characteristic function  $\chi_s$  ( $\chi_s = 1$  inside the body,  $\chi_s = 0$  outside and mollified at the boundary) and its deformation is described by the deformation velocity field associated with the motion pattern under study [32]. Further details, validation and verification of the method can be found in [32, 36]. The computational efficiency of this methodology is enhanced by the use of multiresolution methods in space using wavelets, and in time via local time stepping LTS [41, 33, 34].

We discretize the domain with a multiresolution grid of minimum spacing of  $h^e = L/820$ . The mollification length of  $\chi_s$  is set to  $\epsilon = 2\sqrt{2}h^e$ , Lagrangian CFL to  $LCFL = 0.05$  and penalization factor  $\eta = 10^4$  [32]. The meaning and importance of such parameters are described in detail in [32, 34].

**Results** The results of our simulations are summarized in the Fig. S1. As can be notice, a transition between laminar and flow regime takes place in the range  $10^3 < Sw < 10^4$  (Fig. S1a), consistent with the experimental observations reported in Figure 2 of the main text. Furthermore, our simulations are found to be in agreement with the scaling laws proposed in this work, recovering the exponent  $4/3$  ( $Re = 0.037Sw^{4/3}$  with  $R^2 = 0.999$ ) for laminar flow and the exponent 1 ( $Re = 0.432Sw$  with  $R^2 = 0.999$ ) for the turbulent regime.

For completeness, we illustrate the vorticity field ( $\boldsymbol{\omega} = \nabla \times \mathbf{u}$ ) produced in the flow by the swimmer (Fig. S1b). Furthermore, in (Fig. S1c-d) we report the swimmers' forward and lateral velocities of all simulations used to compile the Fig. S1a.

The agreement of the numerical simulations with the present theory, obtained by varying the flow kinematic viscosity  $\nu$ , supports our simple scaling laws and corresponding hydrodynamic mechanisms.

**Comparison with three-dimensional simulations** We investigate the legitimacy of our two-dimensional approach (modeling and simulations), by comparison with three-dimensional simulations. The data reported here correspond to three-dimensional swimmers characterized by intermediate and high Reynolds numbers, performed and validated via different numerical schemes by several groups [68, 67, 32, 38]. In particular, remeshed vortex methods [32, 38], finite volumes [68] and finite differences [67] were employed. As can be noticed in Fig. S2, three-dimensional simulations confirm our scaling laws in both the laminar and turbulent regime. We find remarkable the fact that simulations performed by several groups [68, 67, 32, 38] employing different numerical techniques scale according to our predictions.

Finally, we turn to both a qualitative and quantitative comparison between 2D and 3D simulations, based on [38]. In this comparison swimmers are characterized by different height profiles, while the width (planar) profile is maintained constant among 2D and 3D simulations. Such study shows how the evolution in time of the swimming velocity present the same dynamic in 2D and 3D (see Fig. S3). Moreover, 2D simulations are also shown to quantitatively capture the absolute value of swimming speeds within  $\sim 10\%$  error, below or comparable to the experimental variability of live fish measurements. These conclusions have been also demonstrated in [36]. This study, which uses both 2D and 3D numerical simulations, confirms the validity of the two-dimensional modeling approach, which is shown to correctly capture the dynamics of complex C-start maneuvers. The comparison of 2D and 3D simulations with experiments shows, even in unsteady situations, how three-dimensional simulations validate the use of two-dimensional models [35], and makes a strong case for the predictive capabilities of 2D simulations.

## 2 Database construction

The experimental studies we used in our analysis refer to a ‘sustained’ regime of locomotion, i.e. at least few consecutive tail beats, disregarding whether the data correspond to cruise swimming or burst swimming. Our theory in fact relates frequency (in the Swimming number - input) to swimming speed (in the Reynolds number - output) through a mechanistic argument. Therefore, as long as a ‘sustained’ motion can be observed, our theory applies both in the case of cruise and burst swimming.

### 2.1 Fish database construction

In this section we report all the raw data for fish used to compile Figure 2 in the main text, and the corresponding sources. As a general notation the normalized tail beat amplitude is referred to as  $\lambda = A/L$ .

**Dace, trout and goldfish** The data reported by Bainbridge [42] for dace (*Leuciscus leuciscus*), trout (*Oncorhynchus mykiss*) and goldfish (*Carassius auratus*) are plotted as  $Re$  versus  $Sw$  in the Fig. S4a. In order to estimate the amplitude used to compile Figure 2 in the main text, for each specimen we computed its average value given the data of [42]. For the specimens whose tail beat amplitude was not reported, we used the mean value of its species.

**Mackerel** The data reported by Hunter et al. [43] for mackerel *Trachurus symmetricus* are summarized in the Fig. S4b. For the specimens whose tail beat amplitude was not reported, we used the mean value  $\lambda = 0.21$  [43].

**Sturgeon** The data reported by Webb [44] for sturgeon *Acipenser fulvescens* of length  $L = 15.7\text{cm}$  are summarized in the Fig. S4c. The tail beat amplitude was set to the average value  $\lambda = 0.19$ , as reported in [44].

**Rainbow trout** The data reported by Webb [45] for rainbow trout *Salmo gairdneri* of length  $L = 20.1\text{cm}$  are summarized in the Fig. S4d. The tail beat amplitude  $A$  used to compile Figure 2 in the main text, was computed by averaging the values given in the Figure 3a illustrated in the original paper [45].

**Giant bluefin tuna** The data reported by Wardle et al. [46] for giant bluefin tuna *Thunnus thynnus* are summarized in the Fig. S5a. The average length was set to  $L = 2.5\text{m}$ , from the range given in [46]. Since, as indicated in [46], the tail beat amplitude varied from  $\lambda = 0.077$  to  $\lambda = 0.235$  for increasing frequencies, we estimated  $\lambda$  from these values using a linear relation.

**Saithe and Mackerel** The data reported by Videler et al. [47] for saithe *Pollachius virens* and mackerel *Scomber scombrus* are summarized in the Fig. S5b. The average length of saithe was set to  $L = 37\text{cm}$ , while the average length of mackerel was set to  $L = 32\text{cm}$ , given the specimens lengths indicated in [47]. The tail beat amplitudes were estimated from lateral displacements illustrated in [47], and quantified as  $\lambda = 0.18$  for saithe and  $\lambda = 0.21$  for mackerel.

**Sharks** The data reported by Webb et al. [48] for nurse shark (*Ginglymostoma cirratum*), leopard shark (*Triakis semifasciata*), lemon shark (*Negaprion brevirostris*), bonnethead shark (*Sphyrna tiburo*), blacktip shark (*Carcharhinus melanopterus*), and bull shark (*Carcharhinus leucas*) are summarized and plotted as  $Re$  versus  $Sw$  in the Fig. S5c. The data are presented in the Table S1a.

**Stingray** The data reported by Rosenberger et al. [49] for stingray *Taeniura lymma* are summarized in the Fig. S5d. The characteristic length  $L$  is defined as the disc width, as proposed in the original paper [49]. In order to compile Figure 2 in the main text, the tail beat amplitude  $\lambda$  of each specimen was computed by averaging the data illustrated in Figure 5b in the original paper [49].

**African lungfish in fluids of varying viscosity by Horner et al.** The data reported by Horner et al. et al. [50] relative to the African lungfish *Protopterus annectens* are plotted as  $Re$  versus  $Sw$  in the Fig. S6a. Tail beat amplitude and speed values are extracted from Figure 3 in the original paper [50]. The length ( $L = 55\text{cm}$ ) is determined as the average value of the fish length range indicated in the original paper [50]. The data are presented in the Table S1b.

**Fish phylogenetic tree** The species considered in this study span the entire fish phylogenetic tree as illustrated in the Fig. S7.

## 2.2 Mammals database construction

In this section we report all the raw data for mammals used to compile Figure 2 in the main text, and the corresponding sources.

**Cetaceans** The data reported by Fish [51] for beluga (*Delphinapterus leucas*,  $L = 3.64\text{m}$ ), killer whale (*Orcinus orca*,  $L = 4.74\text{m}$ ), false killer whale (*Pseudorca crassidens*,  $L = 3.75\text{m}$ ) and dolphin (*Tursiops truncatus*,  $L = 2.61\text{m}$ ) are plotted as  $Re$  versus  $Sw$  in the Fig. S6b.

**Seals** The data reported by Fish et al. [52] for harp seal (*Phoca groenlandica*) and ringed seal (*Phoca hispida*) are plotted as  $Re$  versus  $Sw$  in the Fig. S6c. The data are presented in the Table S1c, where the tail beat amplitude values reported in the original paper [52] correspond to half the amplitude  $A$  as defined in the present work.

**Manatees** The data reported by Kojeszewski et al. [53] for Florida manatee *Trichechus manatus latirostris* are plotted as  $Re$  versus  $Sw$  in the Fig. S6d. The tail beat amplitude was set to  $\lambda = 0.22$  and the characteristic length is based on the average length of the adult manatee  $L = 3.34\text{m}$ , as reported in [53].

**Fin whales** The data reported by Goldbogen et al. [54] for fin whale *Balaenoptera physalus* are summarized in the Table S1d, where the tail beat amplitude was set to  $\lambda = 0.2$ , based on the experimental observations of [55] and the length was set to  $L = 19\text{m}$  based on the average length of an adult fin whale [54]. The corresponding kinematic data are plotted as  $Re$  versus  $Sw$  in the Fig. S8a.

**Blue whales** We extracted one data point for blue whale *Balaenoptera musculus*, based on Calambokidis et al. [56]. The length was set to  $L = 25\text{m}$  based on the average length of an adult blue whale. The speed was set to  $U = 6\text{m/s}$  based on the average cruise velocity of an adult blue whale. The tail beat amplitude was set to  $\lambda = 0.2$ , based on the experimental observations of [55]. The swimming frequency was set to  $f = 0.36\text{Hz}$  based on the average Strouhal number ( $St = 0.3$ ) of marine mammals [55].

**Mammal phylogenetic tree** The species considered in this study span the entire marine mammal phylogenetic tree as illustrated in the Fig. S9.

## 2.3 Birds database construction

**Penguins** The data reported by Sato et al. [57] for emperor penguin (*Aptenodytes forsteri*), king penguin (*Aptenodytes patagonicus*), gentoo penguin (*Pygoscelis papua*), Adelie penguin (*Pygoscelis adeliae*), chin-strap penguin (*Pygoscelis antarctica*), macaroni penguin (*Eudyptes chrysolophus*) and little blue penguin (*Eudyptula minor*) are summarized in the Table S1e. The data reported by Clark et al. [58] for emperor penguin (*Aptenodytes forsteri*), king penguin (*Aptenodytes patagonicus*), African penguin (*Spheniscus demersus*), macaroni penguin (*Eudyptes chrysolophus*), Adelie penguin (*Pygoscelis adeliae*), rockhopper penguin (*Eudyptes crestatus*), and little blue penguin (*Eudyptula minor*) are summarized in the Table S1e. The corresponding kinematic data are plotted as  $Re$  versus  $Sw$  in the Fig. S8. An estimate of the tail beat amplitude was extracted from Fig. 2 of the original paper by Clark et al. [58] and set to  $\lambda = 0.4$ . Characteristic lengths are based on the average adult length of each species.

## 2.4 Amphibians database construction

In this section we report all the raw data for amphibians used to compile Figure 2 in the main text, and the corresponding sources.

**Tadpoles** The data reported by Wassersug et al. [59] for tadpoles of *Rana catesbeiana*, *Rana septentrionalis*, *Rana clamitans* and *Bufo americanus* are plotted as  $Re$  versus  $Sw$  in the Fig. S8c.

## 2.5 Reptiles database construction

In this section we report all the raw data for reptiles used to compile Figure 2 in the main text, and the corresponding sources.

**American alligator** The data reported by Fish [60] for American alligator *Alligator mississippiensis*, are plotted as  $Re$  versus  $Sw$  in the Fig. S8d. Length and amplitude were set, respectively, to  $L = 0.467\text{m}$  and  $\lambda = 0.24$ , as in the original paper [60].

## 2.6 Larvae database construction

In this section we report all the raw data for larvae used to compile Figure 2 in the main text, and the corresponding sources.

**Larval zebrafish by Muller et al.** The data reported by Muller et al. [40] for larval zebrafish *Danio rerio*, are plot as  $Re$  versus  $Sw$  in the Fig. S10a. To compile Figure 2 in the main text, we used both the dataset reported in Table 1 and Figure 7 of the original paper [40]. For the latter dataset, we estimated  $\lambda$  by averaging the values of the Table S1f.

**Larval zebrafish by Green et al.** The data reported by Green et al. [61] for larval zebrafish *Danio rerio*, are plotted as  $Re$  versus  $Sw$  in the Fig. S10b. Tail beat frequency was observed to be constant  $f = 30\text{Hz}$  in the set of experiments of [61].

**Ascidian larvae** The data reported by McHenry et al. [62, 63] for Ascidian larvae *Distaplia occidentalis* [62] and *Aplidium constellatum* [63] are plotted as  $Re$  versus  $Sw$  in the Fig. S10b. Due to the lack of information regarding the tail beat amplitude, we set  $\lambda = 0.2$  consistently with [61, 40]. Data for Ascidian larvae *Ciona intestinalis* in [62] were omitted since their Reynolds numbers are below the minimum value for our theory to hold ( $Re \simeq 10$ ).

**Larval zebrafish** We extracted two data points for larval zebrafish *Brachydanio rerio*, based on Figure 7 and 8 of the reference [64]. Data are summarized in the Table S1h.

## 2.7 Mayfly larvae

We extracted one data point for mayfly larvae *Chloeon dipterous*, based on Brackenbury et al. [65]. Data are summarized in the Table S1i.

### 3 Statistical data analysis

The statistical data analysis performed in order to validate our hydrodynamic theory is summarized in the Fig. S11. For each entry of the Fig. S11 we report the best fit power law  $Re = bSw^a$ , where  $a$  and  $\log(b)$  represent, respectively, the slope and intercept of the best fit line in a log log scale, and the corresponding coefficient of determination  $R^2$ .

### 4 Credits for photographs of swimmers

We wish to thank the authors of the photographs used to compile Figure 1 in the main text, for making their work available. The credits are listed below.

- **Ascidian larva.** Source: [http://invert-embryo.blogspot.com/2013/06/ascidian-tadpole-larvae-settlement-and\\_6.html](http://invert-embryo.blogspot.com/2013/06/ascidian-tadpole-larvae-settlement-and_6.html). Article: Ascidian tadpole larvae: settlement and metamorphosis. Authors: Students of Comparative Embryology and Larval Biology course taught by Dr. Svetlana Maslakova at the Oregon Institute of Marine Biology in Charleston, Oregon (USA).
- **Mayfly larva.** Source: <http://notes-from-dreamworlds.blogspot.com/>. Author: Daniel Stoupin.
- **Zebrafish larva.** Source: <http://www.genome.gov/pressDisplay.cfm?photoID=95>, Wikipedia Commons. Authors: Shawn Burgess, NHGRI.
- **Amphibian tadpole.** Source: Wikipedia Commons. Author: Miika Silfverberg from Vantaa, Finland.
- **Stingray.** Source: <http://www.biolib.cz/cz/image/id200316/>. Author: Viktor Vrbovsky.
- **Dace.** Source: Wikipedia Commons. Author: Hans Hillewaert.
- **Shark.** Source: <http://www.free-picture.net>
- **Goldfish.** Source: <http://english.turkcebilgi.com/gold+fish>, Wikipedia Commons. Author: Lerd-suwa.
- **Crocodile.** Source: [http://www.nasa.gov/centers/kennedy/images/content/91159main\\_93pc780.jpg](http://www.nasa.gov/centers/kennedy/images/content/91159main_93pc780.jpg), Wikipedia Commons.
- **Penguin.** Source: Wikipedia Commons. Author: Samuel Blanc.
- **Killer whale.** Source: <http://walldie.com/orca-whale-wallpapers-hd/>
- **Manatee.** Source: Wikipedia Commons. Author: Reid, Jim P., U.S. Fish and Wildlife Service.
- **Beluga.** Source: <http://www.georgiaaquariumblog.org/georgia-aquarium-blog/2012/6/29/beluga-whale-acquisition.html>
- **Blue whale.** Source: <http://www.earthwindow.com/blue.html>. Author: Mike Johnson.

### References

31. M. Coquerelle and G.H. Cottet. A vortex level set method for the two-way coupling of an incompressible fluid with colliding rigid bodies. *Journal of Computational Physics*, 227(21):9121–9137, 2008.
32. M. Gazzola, P. Chatelain, W.M. van Rees, and P. Koumoutsakos. Simulations of single and multiple swimmers with non-divergence free deforming geometries. *Journal of Computational Physics*, 230(19):7093–7114, 2011.
33. M. Gazzola, C. Mimeau, A.A. Tchieu, and P. Koumoutsakos. Flow mediated interactions between two cylinders at finite re numbers. *Physics of Fluids*, 24(4):043103, 2012.
34. M. Gazzola, B. Hejazialhosseini, and P. Koumoutsakos. Reinforcement learning and wavelet adapted vortex methods for simulations of self-propelled swimmers. *Accepted by SIAM Scientific Computing*, 2014.
35. M.S. Triantafyllou. Survival hydrodynamics. *Journal of Fluid Mechanics*, 698:1–4, 2012.

36. M. Gazzola, W.M. Van Rees, and P. Koumoutsakos. C-start: optimal start of larval fish. *Journal of Fluid Mechanics*, 698:5–18, 2012.
37. M. Gazzola, O.V. Vasilyev, and P. Koumoutsakos. Shape optimization for drag reduction in linked bodies using evolution strategies. *Computers and Structures*, 89(11-12):1224–1231, 2011.
38. W.M. van Rees, M. Gazzola, and P. Koumoutsakos. Optimal shapes for anguilliform swimmers at intermediate reynolds numbers. *Journal of Fluid Mechanics*, 722, 2013.
39. J. Carling, T. L. Williams, and G. Bowtell. Self-propelled anguilliform swimming: Simultaneous solution of the two-dimensional navier-stokes equations and newton's laws of motion. *Journal of Experimental Biology*, 201(23):3143–3166, 1998.
40. U.K. Muller and J.L. van Leeuwen. Swimming of larval zebrafish: ontogeny of body waves and implications for locomotory development. *Journal of Experimental Biology*, 207(5):853–868, 2004.
41. B. Hejazialhosseini, D. Rossinelli, M. Bergdorf, and P. Koumoutsakos. High order finite volume methods on wavelet-adapted grids with local time-stepping on multicore architectures for the simulation of shock-bubble interactions. *Journal of Computational Physics*, 229(22):8364–8383, 2010.
42. R. Bainbridge. The speed of swimming of fish as related to size and to the frequency and amplitude of the tail beat. *Journal of Experimental Biology*, 35(1):109–133, 1958.
43. J.R. Hunter and J.R. Zweifel. Swimming speed, tail beat frequency, tail beat amplitude, and size in jack mackerel, *trachurus-symmetricus*, and other fishes. *Fishery Bulletin of the National Oceanic and Atmospheric Administration*, 69(2):253–267, 1971.
44. P.W. Webb. Kinematics of lake sturgeon, *acipenser fulvescens*, at cruising speeds. *Canadian Journal of Zoology*, 64(10):2137–2141, 1986.
45. P.W. Webb. Steady swimming kinematics of tiger musky, an esociform accelerator, and rainbow-trout, a generalist cruiser. *Journal of Experimental Biology*, 138:51–69, 1988.
46. C.S. Wardle, J.J. Videler, T. Arimoto, J.M. Franco, and P. He. The muscle twitch and the maximum swimming speed of giant bluefin tuna, *thunnus thynnus* l. *Journal of fish biology*, 35(1):129–137, 1989.
47. J.J. Videler and F. Hess. Fast continuous swimming of two pelagic predators, saithe (*pollachius virens*) and mackerel (*scomber scombrus*): a kinematic analysis. *Journal of Experimental Biology*, 109(1):209–228, 1984.
48. P.W. Webb and R.S. Keyes. Swimming kinematics of sharks. *Fishery Bulletin*, 80(4):803–812, 1982.
49. L.J. Rosenberger and M.W. Westneat. Functional morphology of undulatory pectoral fin locomotion in the stingray *taeniura lymma* (chondrichthyes: dasyatidae). *Journal of Experimental Biology*, 202(24):3523–3539, 1999.
50. A.M. Horner and B.C. Jayne. The effects of viscosity on the axial motor pattern and kinematics of the african lung-fish (*protopterus annectens*) during lateral undulatory swimming. *Journal of Experimental Biology*, 211(10):1612–1622, 2008.
51. F.E. Fish. Comparative kinematics and hydrodynamics of odontocete cetaceans: morphological and ecological correlates with swimming performance. *The Journal of Experimental Biology*, 201(20):2867–2877, 1998.
52. F.E. Fish, S. Innes, and K. Ronald. Kinematics and estimated thrust production of swimming harp and ringed seals. *Journal of Experimental Biology*, 137(1):157–173, 1988.
53. T. Kojaszewski and F.E. Fish. Swimming kinematics of the florida manatee (*trichechus manatus latirostris*): hydrodynamic analysis of an undulatory mammalian swimmer. *Journal of Experimental Biology*, 210(14):2411–2418, 2007.
54. J.A. Goldbogen, J. Calambokidis, R.E. Shadwick, E.M. Oleson, M.A. McDonald, and J.A. Hildebrand. Kinematics of foraging dives and lunge-feeding in fin whales. *Journal of Experimental Biology*, 209(7):1231–1244, 2006.
55. J.J. Rohr and F.E. Fish. Strouhal numbers and optimization of swimming by odontocete cetaceans. *Journal of Experimental Biology*, 207(10):1633–1642, 2004.
56. J. Calambokidis and G.H. Steiger. *Blue whales*. Voyager Press Inc., Duluth, Minn, 1997.
57. K. Sato, K. Shiomi, Y. Watanabe, Y. Watanuki, A. Takahashi, and P.J. Ponganis. Scaling of swim speed and stroke frequency in geometrically similar penguins: they swim optimally to minimize cost of transport. *Proceedings of the Royal Society B: Biological Sciences*, 277(1682):707–714, 2010.

58. B.D. Clark and W. Bemis. Kinematics of swimming of penguins at the detroit zoo. *Journal of Zoology*, 188:411–428, 1979.
59. R.J. Wassersug and K.S. Hoff. The kinematics of swimming in anuran larvae. *Journal of Experimental Biology*, 119(1):1–30, 1985.
60. F.E. Fish. Kinematics of undulatory swimming in the american alligator. *Copeia*, pages 839–843, 1984.
61. M.H. Green, R.K. Ho, and M.E. Hale. Movement and function of the pectoral fins of the larval zebrafish (*danio rerio*) during slow swimming. *The Journal of experimental biology*, 214(18):3111–3123, 2011.
62. M.J. McHenry. The morphology, behavior, and biomechanics of swimming in ascidian larvae. *Canadian journal of zoology*, 83(1):62–74, 2005.
63. M.J. McHenry and J. Strother. The kinematics of phototaxis in larvae of the ascidian aplidium constellatum. *Marine Biology*, 142(1):173–184, 2003.
64. S. A. Budick and D. M. O'Malley. Locomotor repertoire of the larval zebrafish: swimming, turning and prey capture. *Journal of Experimental Biology*, 203(17):2565–2579, 2000.
65. J. Brackenbury. Kinematics and hydrodynamics of swimming in the mayfly larva. *Journal of experimental biology*, 207(6):913–922, 2004.
66. G.K. Taylor, R.L. Nudds, and A.L.R. Thomas. Flying and swimming animals cruise at a strouhal number tuned for high power efficiency. *Nature*, 425(6959):707–711, 2003.
67. E.D. Tytell, I. Borazjani, F. Sotiropoulos, T.V. Baker, E.J. Anderson, and G.V. Lauder. Disentangling the functional roles of morphology and motion in the swimming of fish. *Integrative and Comparative Biology*, 50(6):1140–1154, 2010.
68. S. Kern and P. Koumoutsakos. Simulations of optimized anguilliform swimming. *Journal of Experimental Biology*, 209(24):4841–4857, 2006.
69. R.R. Betancur, R.E. Broughton, E.O. Wiley, K. Carpenter, J.A. Lopez, C. Li, N.I. Holcroft, D. Arcila, M. Sanciango, J.C. Cureton II, F. Zhang, T. Buser, M.A. Campbell, J.A. Ballesteros, A. Roa-Varon, S. Willis, W.C. Borden, T. Rowley, P.C. Reneau, D.J. Hough, G. Lu, T. Grande, G. Arratia, and G. Orti. The tree of life and a new classification of bony fishes. *PLOS Currents Tree of Life*, 2013.
70. M.S. Springer, M.J. Stanhope, O. Madsen, and W.W. de Jong. Molecules consolidate the placental mammal tree. *Trends in Ecology and Evolution*, 19(8):430 – 438, 2004.

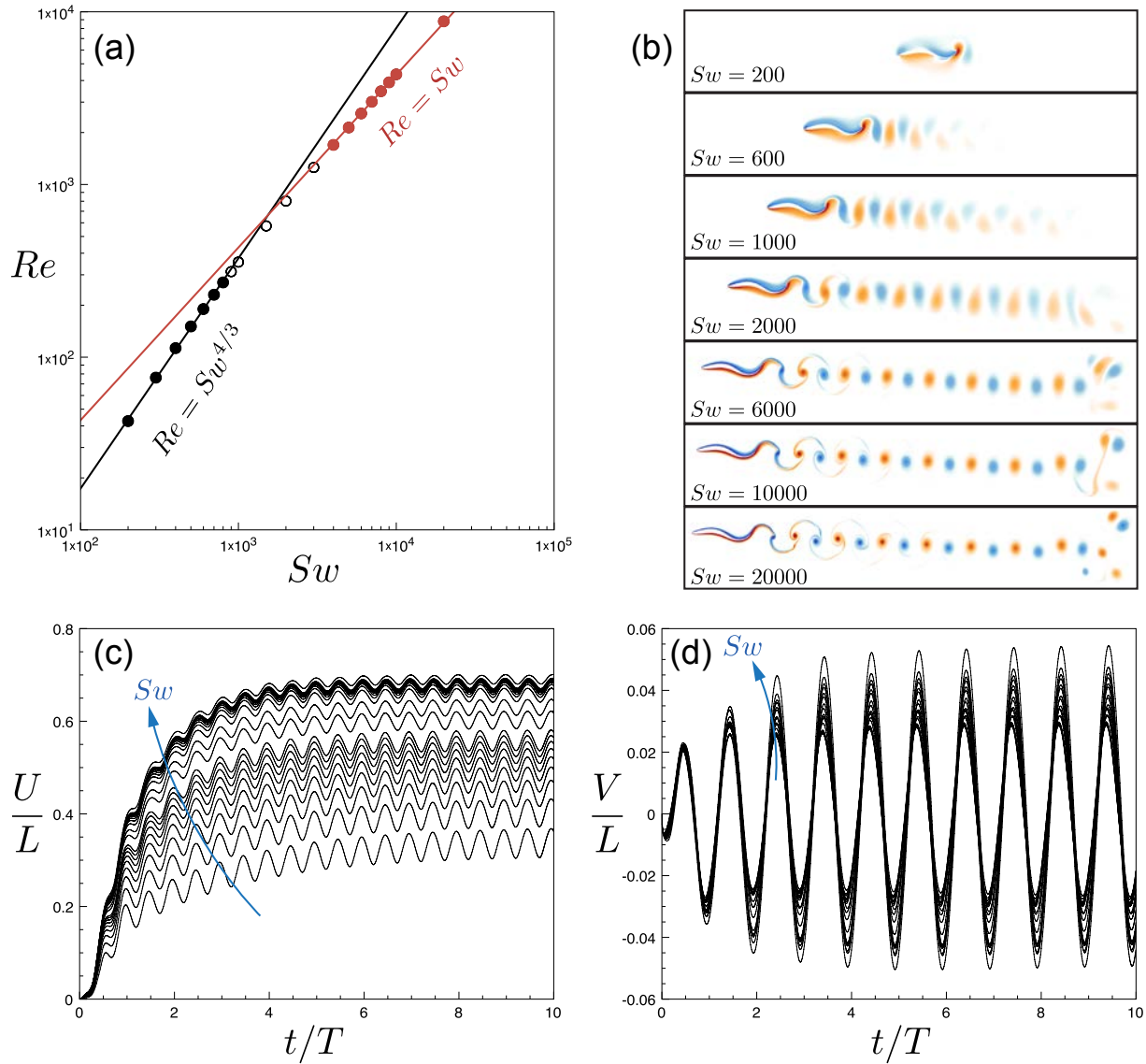


**Fig. S1: Simulation of swimmers in fluids with varying viscosity.** (a) Simulation results are plotted as  $Re$  versus  $Sw$  to assess the validity of the proposed scaling laws. (b) Vorticity fields at time  $t = 10T$  produced by swimmers with different  $Sw$ . Red and blue colors correspond, respectively, to positive and negative vorticity values. (c-d) Time evolution of forward ( $U$ ) and lateral ( $V$ ) velocities of all simulated swimmers. Each curve corresponds to a data point in (a).

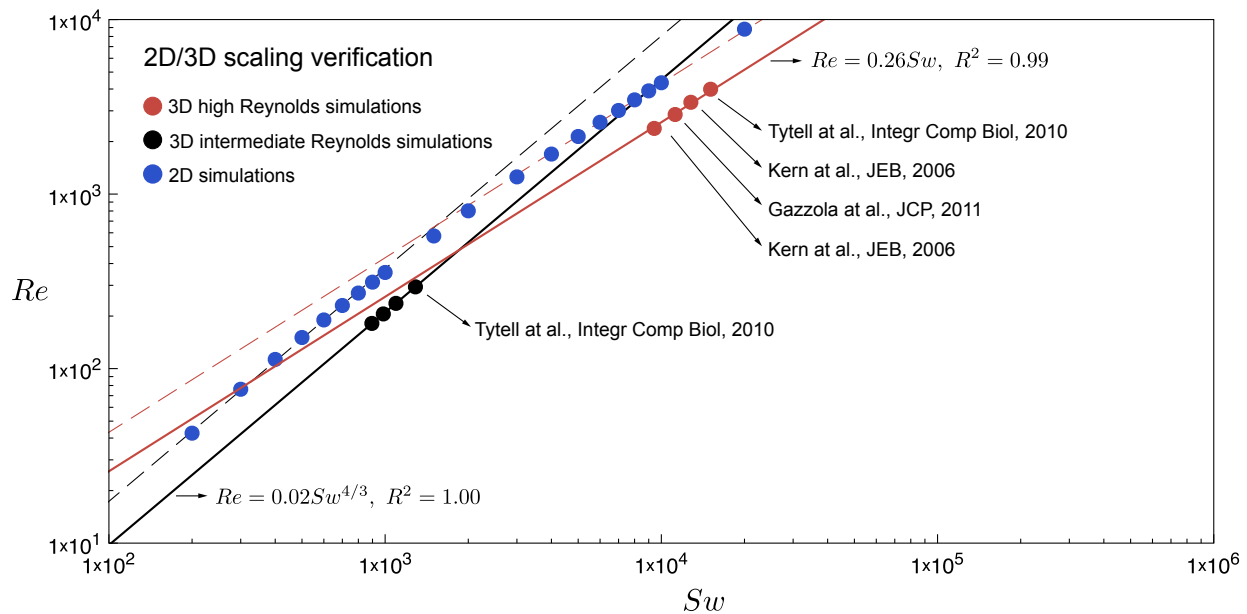


**Fig. S2: Scaling of 2D and 3D simulations.** (a) Two- and three-dimensional simulations confirm the proposed scaling law. Blue dots represent the 2D simulations of Figure 3 in the main text for an anguilliform swimmer whose shape is optimized for speed [38]. The black dot at  $Re=300$  corresponds to the 3D simulation of a mackerel of [67]. The unlabeled dots refer to a three-dimensional efficient swimmer of shape  $\beta_w = \{0.24, 0.3, 0.008, 0.006\}$  and  $\beta_h = \{0.22, 0.27, 0.28, 0.3, 0.3, 0.22\}$  (see the notation of [38]) and characterized by tail beat periods  $T = \{0.9, 1, 1.1\}$ , amplitude  $A = 0.285$ ,  $L = 1$  and  $\nu = 1/550$ . Simulations were performed with a resolution of 500 points across the swimmer's length and  $LCFL = 0.1$  (credit to van Rees and Koumoutsakos). The velocity used to compute the corresponding  $Re$  is the final speed at  $t = 6.5T$ . Red dots correspond to a 3D simulation of mackerel at  $Re=4000$  [67], optimized fast and efficient eel-like swimmers [68] and anguilliform swimmer [32]. As can be noticed 3D simulations confirm our power law both in the laminar (fit characterized by  $R^2 = 1.00$ ) and turbulent regime (fit characterized by  $R^2 = 0.99$ ). Remarkably, simulations performed with completely different numerical techniques scale as predicted, giving us additional confidence on the correctness of our approach.

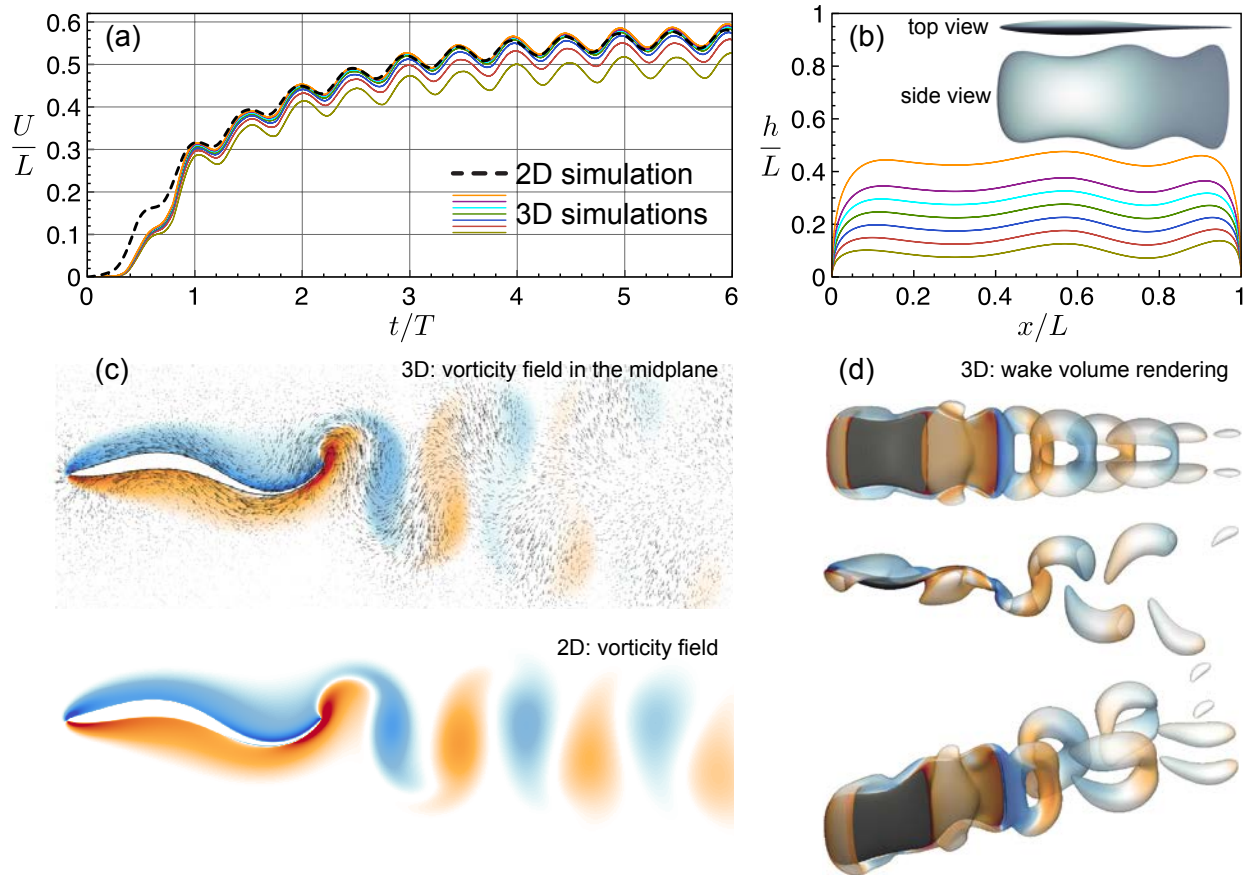


**Fig. S3: Quantitative comparison of 2D and 3D simulations.** Here we use the results of previous computations for optimal fast swimmers [38] to quantitatively justify the use of 2D simulations for the validation of the proposed scaling law. Three-dimensional shapes are constructed by ellipsoidal cross-sections with half-axes defined by the width (top view in b) and the height (side view in b) profiles. Several 3D anguilliform swimmers characterized by the same width profile (top panel in b) but with different height profiles (bottom panel in b). (a) The transient evolution of the forward velocity in time ( $T$  is the tail oscillation period) of each 3D simulation corresponds to the matched color code of the swimmer profiles shown in panel (b). The dashed black line corresponds instead to a 2D simulation with a 2D swimmer of width profile identical to the 3D fish. We see that the 2D model simulations match the 3D simulations for all the profiles used within a  $\sim 10\%$  difference. This difference is generally below or at least comparable with the variability observed in the over 1000 experiments reported in this work. Moreover, the qualitative evolution of the swimming velocity in time is preserved from 3D to 2D. From a mathematical point of view this means that our theoretically derived power laws are not affected by the dimension; offsets in swimming velocities when moving from 2D to 3D change the prefactor and not the exponent. (c) The vorticity field (blue negative, red positive values) of a 2D simulation at  $Re=550$  is shown next to the vorticity field in the mid-plane of a 3D simulation at  $Re=550$ . As can be seen the main mid-plane features of the three-dimensional wake (vortex cores shedding - image courtesy of van Rees and Koumoutsakos) are preserved in 2D, thus validating our hypothesis that this captures the leading order dynamics of swimming. (d) Volume rendering of the wake associated with a 3D swimmer at  $Re=550$  (image adapted from [38]). All simulations are carried out assuming 500 points across the fish length, and  $LCFL=0.1$ . More details about the simulation techniques can be found in [38].

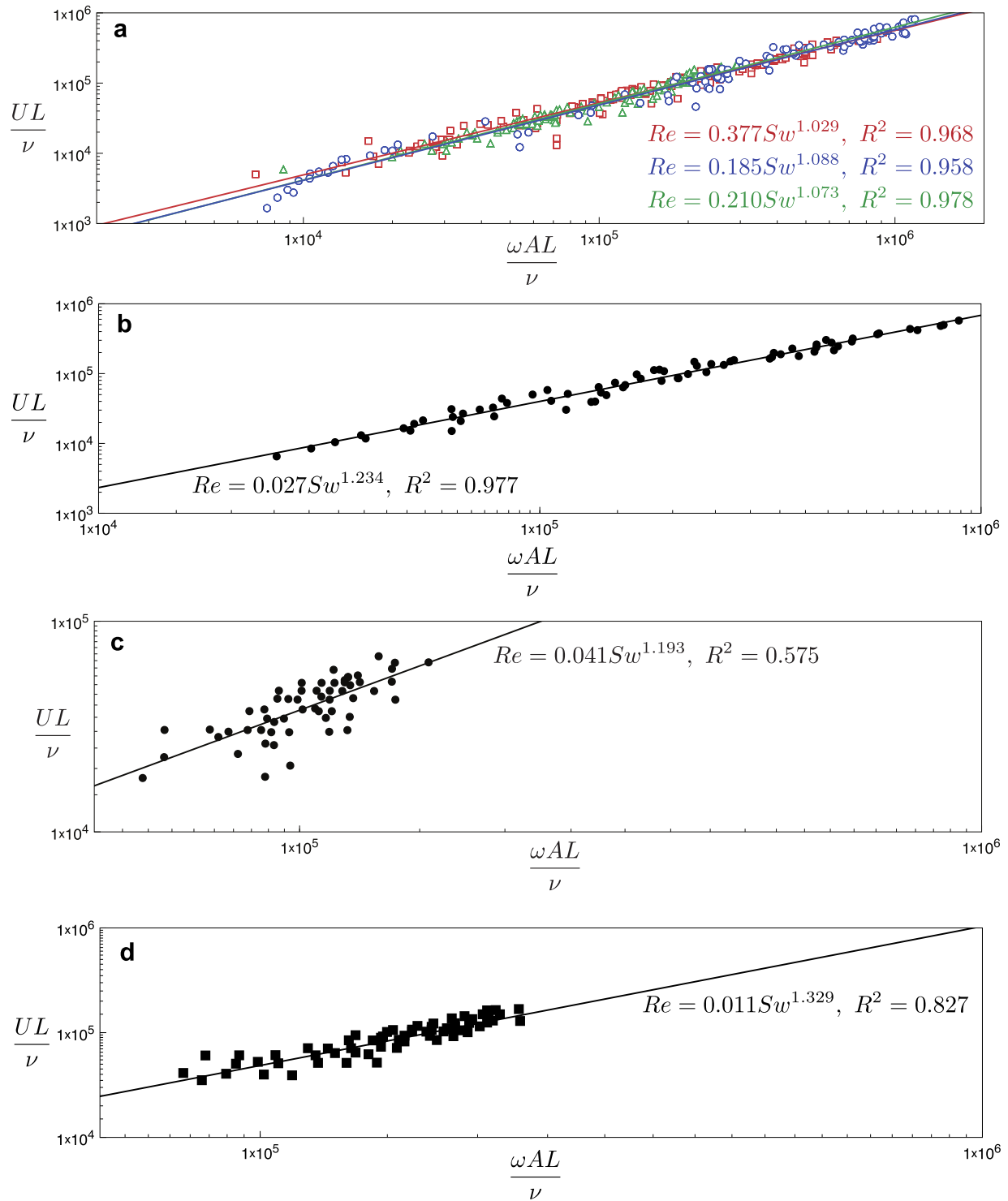


**Fig. S4:** Data reported by various authors and corresponding best fit lines (see Section 3) are plotted as  $Re$  versus  $Sw$ . **a** Dace ( $\square$ ), trout ( $\circ$ ) and goldfish ( $\triangle$ ) [42]. **b** Mackerel *Trachurus symmetricus* [43] **c** Sturgeon *Acipenser fulvescens* [44] **d** Rainbow trout [45]

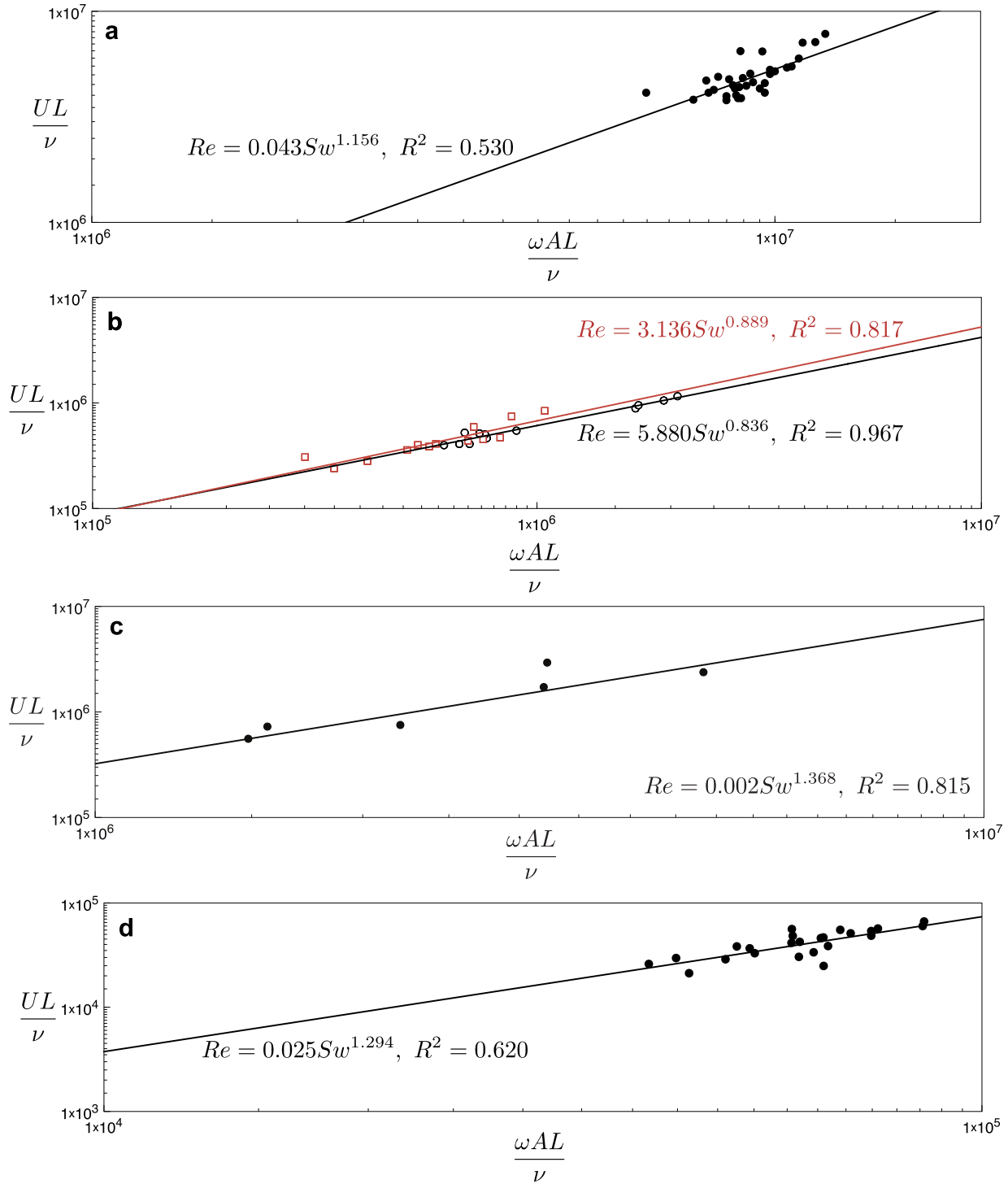


**Fig. S5: Data reported by various authors and corresponding best fit lines (see Section 3) are plotted as  $Re$  versus  $Sw$ . a Giant bluefin tuna *Thunnus thynnus* [46]. b Saithe *Pollachius virens* ( $\square$ ) and mackerel *Scomber scombrus* ( $\circ$ ) [47] c Several species of sharks [48]. d Stingrays *Taeniura lymma* with characteristic length  $L = 14.3\text{cm}$  [49].**

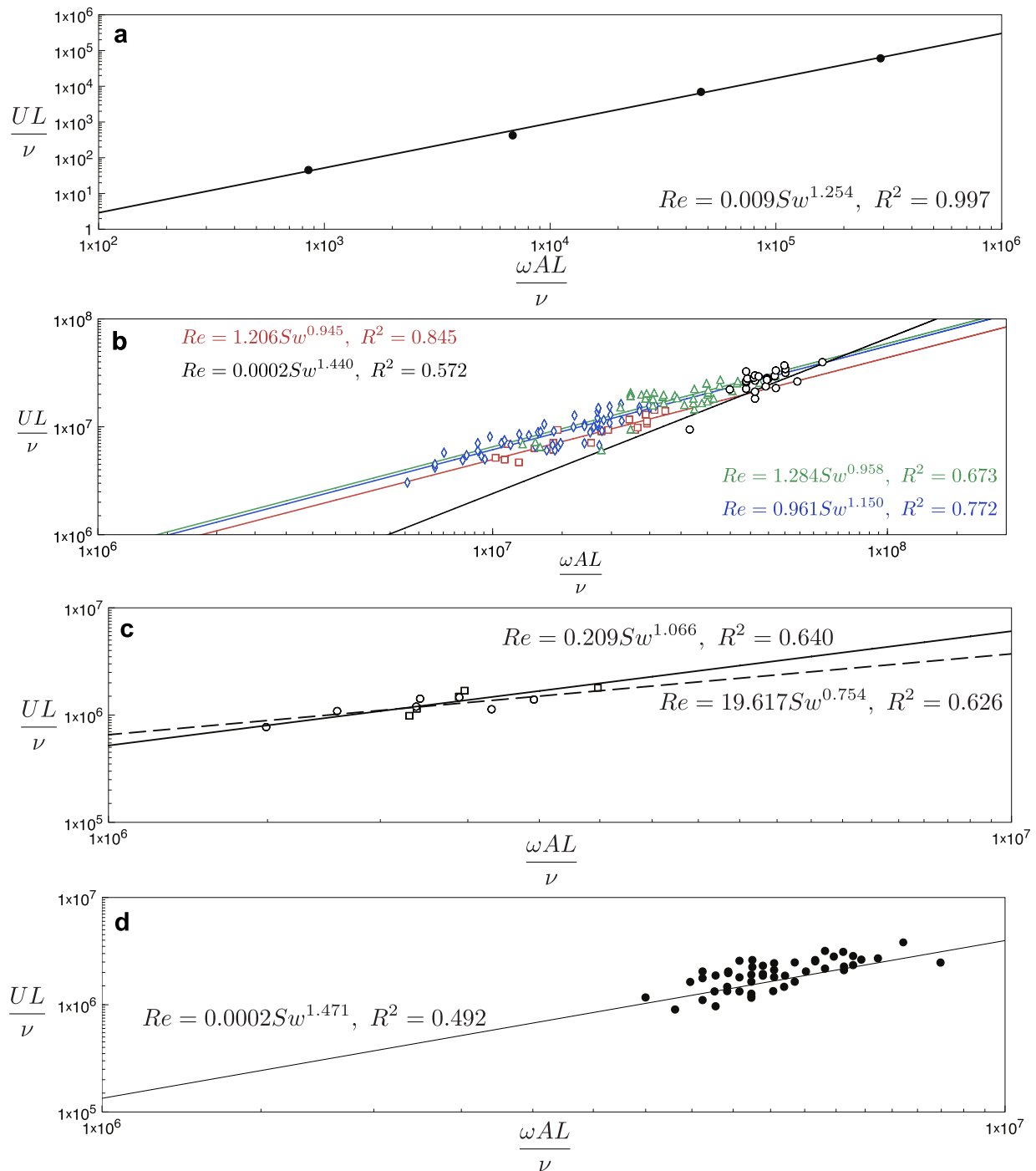


**Fig. S6: Data reported by various authors and corresponding best fit lines (see Section 3) are plotted as  $Re$  versus  $Sw$ .** **a** African lungfish *Protopterus annectens* subject to fluid viscosity variations [50]. **b** Beluga (*Delphinapterus leucas*) ( $\square$ ), killer whale (*Orcinus orca*) ( $\circ$ ), false killer whale (*Pseudorca crassidens*) ( $\triangle$ ), and dolphin (*Tursiops truncatus*) ( $\diamond$ ) [51]. **c** Harp seal ( $\square$ ) and ringed seal ( $\circ$ ) [52]. **d** Florida manatee *Trichechus manatus latirostris* [53].

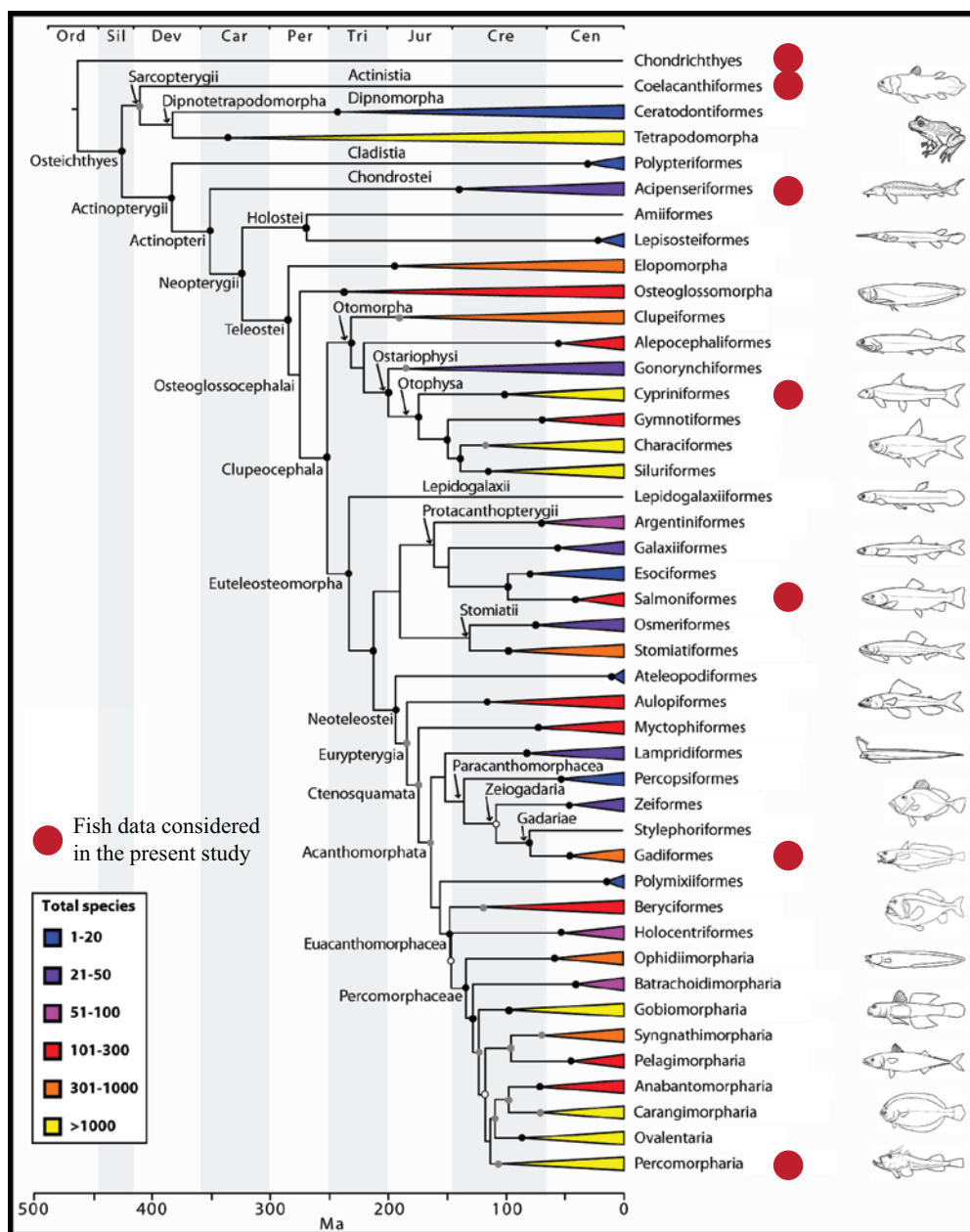
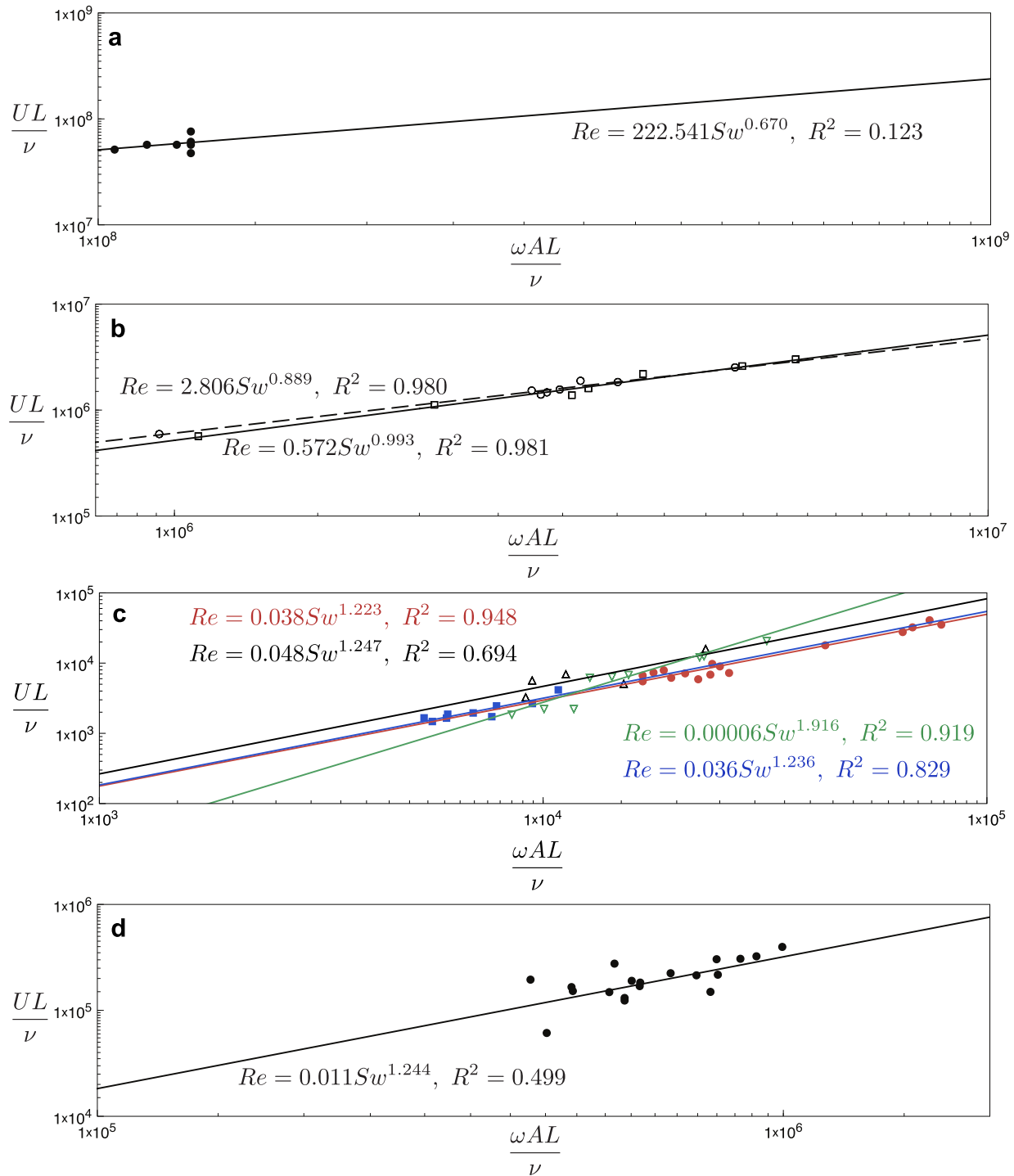
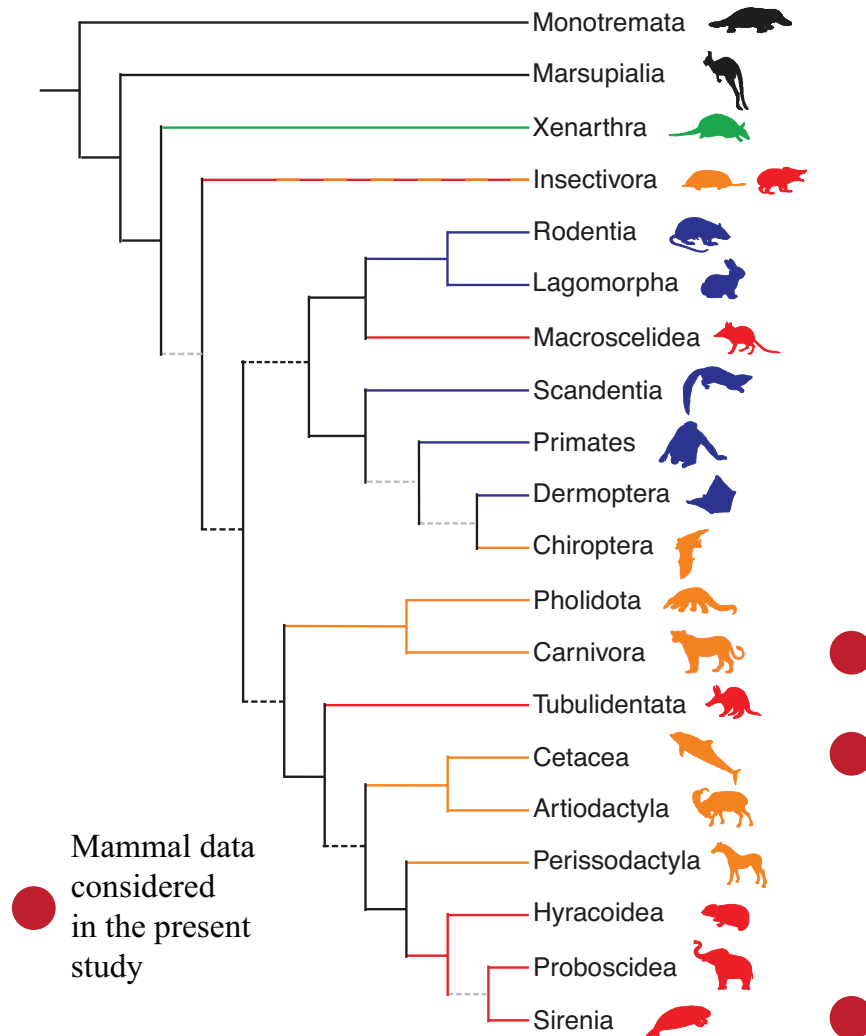


Fig. S7: Fish phylogenetic tree and species considered in the present study. Image adapted from [69].



**Fig. S8:** Data reported by various authors and corresponding best fit lines (see Section 3) are plotted as  $Re$  versus  $Sw$ . **a** Fin whale *Balaenoptera physalus* [54]. **b** Penguin data [57] ( $\circ$ ), [58] ( $\square$ ) with corresponding best fit lines (dashed line for data of [57] and solid line for data of [58]). **c** Tadpole data [59], *Rana catesbeiana* for organisms of average length  $L = 6\text{ cm}$  ( $\bullet$ ), *Rana septentrionalis* of average length  $L = 4.75\text{ cm}$  ( $\triangle$ ), *Rana clamitans* of average length  $L = 5.25\text{ cm}$  ( $\nabla$ ), and *Bufo americanus* of average length  $L = 2.23\text{ cm}$  ( $\blacksquare$ ). **d** American alligator *Alligator mississippiensis* [60].



**Fig. S9: Mammal phylogenetic tree and species considered in the present study.** Image adapted from [70].

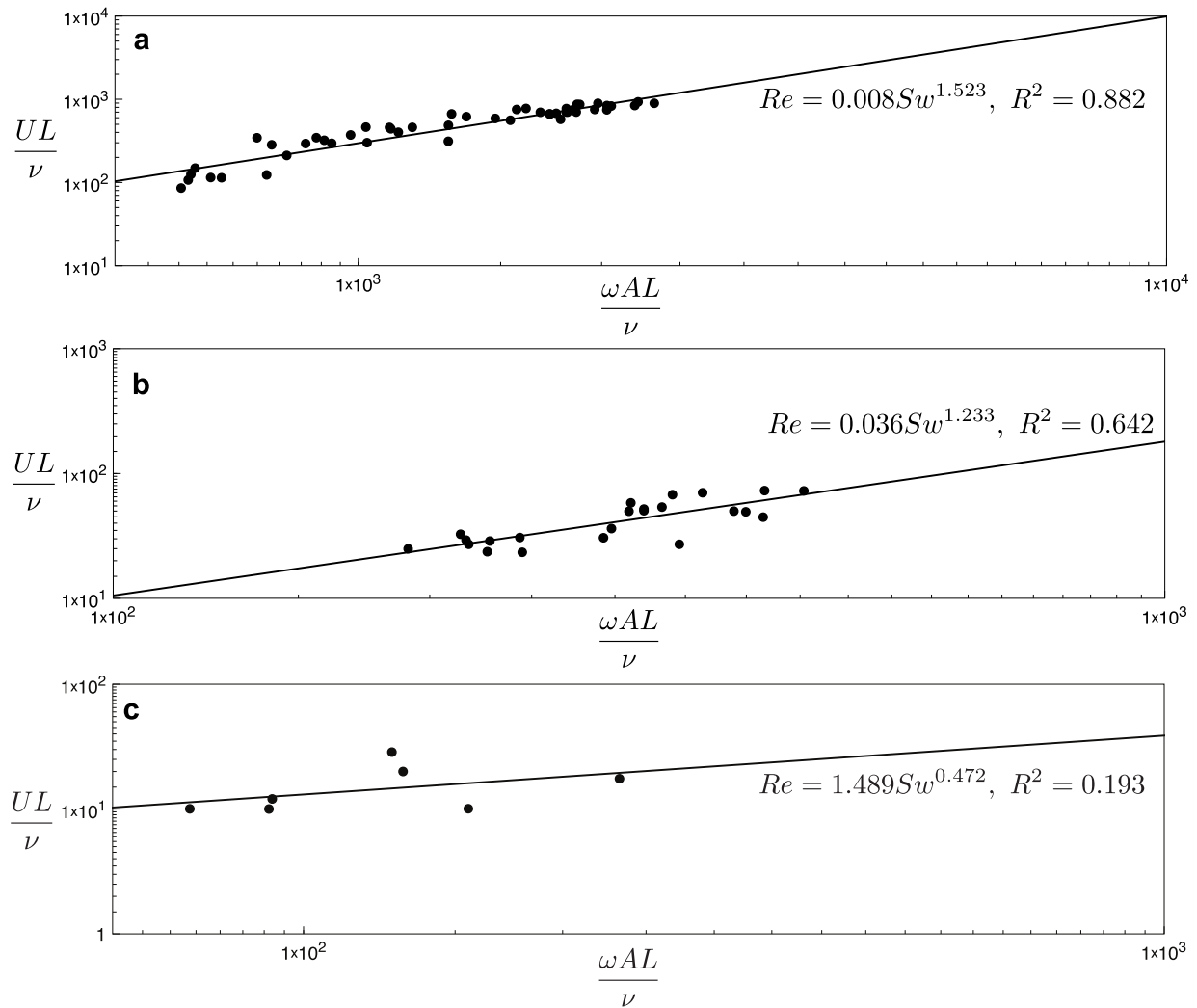


**Fig. S10:** Data reported by various authors and corresponding best fit lines (see Section 3) are plotted as  $Re$  versus  $Sw$ . **a** Larval zebrafish *Danio rerio* [40]. **b** Larval zebrafish *Danio rerio* [61]. **c** Ascidian larvae [62, 63].

SOURCE	DATA SET	SLOPE	INTERCEPT	R2	N SAMPLES
	LAMINAR (Sw < 10 <sup>4</sup> )	1.310	0.029	0.946	100
	TURBULENT (Sw > 10 <sup>4</sup> )	1.018	0.400	0.985	902
	FISH	1.051	0.281	0.968	635
	AMPHIBIANS	1.219	0.044	0.906	39
	REPTILES	1.244	0.011	0.499	19
	MAMMALS	1.124	0.065	0.939	212
	BIRDS	0.943	1.232	0.976	15
	LARVAE	1.522	0.008	0.956	82
	10 <sup>4</sup> < Sw < 10 <sup>7</sup>	1.004	0.473	0.968	757
	10 <sup>5</sup> < Sw < 10 <sup>8</sup>	1.006	0.485	0.980	668
	10 <sup>6</sup> < Sw < 10 <sup>9</sup>	1.061	0.193	0.945	275
Bainbridge	DACE	1.029	0.377	0.968	153
Bainbridge	GOLDFISH	1.088	0.185	0.958	100
Bainbridge	TROUT	1.073	0.210	0.978	103
Hunter	MACKEREL	1.234	0.027	0.977	70
Webb	TROUT	1.329	0.011	0.827	64
Webb	STURGEON	1.193	0.041	0.575	57
Wardle	TUNA	1.156	0.043	0.530	33
Videler	SAITHE	0.889	3.136	0.817	13
Videler	MACKEREL	0.836	5.880	0.967	12
Webb	SHARKS	1.368	0.002	0.815	6
Rosenberger	STINGRAY	1.294	0.025	0.620	24
	<b>TOTAL</b>				<b>635</b>
Wassersug	TADPOLE RANA CATESBEIANA	1.223	0.038	0.948	16
Wassersug	TADPOLE RANA SEPTENTRIONALIS	1.247	0.048	0.694	5
Wassersug	TADPOLE RANA CLAMITANS	1.916	0.00006	0.919	9
Wassersug	TADPOLE BUFO AMERICANUS	1.236	0.036	0.826	9
	<b>TOTAL</b>				<b>39</b>
Fish	ALLIGATOR	1.244	0.011	0.499	19
	<b>TOTAL</b>				<b>19</b>
Fish	BELUGA	0.945	1.206	0.845	19
Fish	KILLER WHALE	1.440	0.0002	0.572	28
Fish	FALSE KILLER WHALE	0.958	1.284	0.673	42
Fish	DOLPHIN	0.961	1.150	0.772	53
Fish	RINGED SEAL	0.754	19.617	0.626	7
Fish	HARP SEAL	1.066	0.209	0.640	5
Kojeszewski	MANATEE	1.471	0.0002	0.492	50
Goldbogen	FIN WHALE	0.670	222.541	0.123	7
Calambokidis	BLUE WHALE	*	*	*	1
	<b>TOTAL</b>				<b>212</b>
Clark	PENGUINS	0.993	0.572	0.981	7
Sato	PENGUINS	0.889	2.806	0.980	8
	<b>TOTAL</b>				<b>15</b>
Muller	ZEBRAFISH LARVAE	1.523	0.008	0.882	49
Green	ZEBRAFISH LARVAE	1.233	0.036	0.642	23
McHenry	ASCIDIAN LARVAE	0.472	1.489	0.193	7
Brackenbury	MAYFLY LARVAE	*		*	1
Budick	ZEBRAFISH LARVAE	*		*	2
	<b>TOTAL</b>				<b>82</b>

Fig. S11: Statistical data analysis.

<b>a</b>	Length (m)	Ampl. (L)	Freq. (Hz)	Speed (L s <sup>-1</sup> )
Nurse shark	2.25	0.21	0.67	0.34
Leopard shark	0.98	0.20	1.12	0.58
Lemon shark	2.25	0.18	0.95	0.47
Bonnethead shark	0.93	0.18	1.25	0.84
Blacktip shark	0.97	0.18	1.13	0.80
Bull shark	2.25	0.16	0.78	0.58

<b>c</b>	Length (m)	Ampl. (m)	Freq. (Hz)	Speed (m s <sup>-1</sup> )
Ringed seal	1.03	0.15	0.77	0.75
	1.09	0.12	1.09	1.00
	1.03	0.18	1.14	1.10
	1.09	0.16	1.00	1.10
	1.09	0.18	1.20	1.28
	1.03	0.15	1.14	1.38
	1.03	0.15	1.26	1.42
Harp seal	1.64	0.19	0.55	0.60
	1.64	0.15	0.71	0.70
	1.43	0.17	0.80	1.04
	1.43	0.15	0.92	1.18
	1.43	0.17	1.14	1.26

<b>e</b>	Length (cm)	Freq. (Hz)	Speed (m s <sup>-1</sup> )
Emperor penguin	115	1.47	2.2
King penguin	90	1.35	1.7
	90	1.55	2.1
Gentoo penguin	80	2.18	2.3
Adelie penguin	70	2.33	2.1
Chinstrap penguin	68	2.56	2.3
Macaroni penguin	70	2.29	2.0
Little blue penguin	33	3.50	1.8
Emperor penguin	115	1.50	2.26
King penguin	90	2.85	3.35
African penguin	68	3.24	3.23
Macaroni penguin	70	2.62	2.29
Adelie penguin	70	2.50	1.98
Rockhopper penguin	51	3.13	2.18
Little blue penguin	33	3.91	1.72

<b>g</b>	Length (mm)	Ampl. (L)	Freq. (Hz)	Speed (mm s <sup>-1</sup> )
<i>Distaplia occidentalis</i>	2.6	0.2	18.2	3.9
	2.0	0.2	18.2	5.0
	1.8	0.2	18.2	5.6
	2.0	0.2	18.2	6.0
	2.4	0.2	18.2	8.4
	3.2	0.2	18.2	5.5
<i>Aplidium constellatum</i>	2.0	0.2	25.2	14.3

<b>b</b>	Length (cm)	Ampl. (L)	Freq. (Hz)	Speed (L s <sup>-1</sup> )
$\nu = 10^{-6} \text{m}^2/\text{s}$	55	0.10	0.83	0.20
$\nu = 10^{-5} \text{m}^2/\text{s}$	55	0.11	1.20	0.23
$\nu = 10^{-4} \text{m}^2/\text{s}$	55	0.14	1.44	0.14
$\nu = 10^{-3} \text{m}^2/\text{s}$	55	0.13	1.94	0.15

<b>d</b>	Length (m)	Ampl. (L)	Freq. (Hz)	Speed (m s <sup>-1</sup> )
Fin whale	19	0.2	0.28	3.0
	19	0.2	0.28	4.0
	19	0.2	0.25	3.0
	19	0.2	0.27	3.0
	19	0.2	0.28	2.5
	19	0.2	0.28	3.2
	19	0.2	0.23	2.7
	19	0.2	0.23	2.7

<b>f</b>	Length (mm)	Ampl. (L)	Freq. (Hz)	Speed (L s <sup>-1</sup> )
Larval zebrafish	3.5	0.22	40	9.3
	3.5	0.20	71	37.5
	3.9	0.26	31	8.1
	3.9	0.23	100	55.3
	4.2	0.24	68	43.8
	4.3	0.19	42	16.0
	4.3	0.25	80	48.4
	4.4	0.11	56	17.8
	4.4	0.21	73	44.9

<b>h</b>	Length (mm)	Ampl. (L)	Freq. (Hz)	Speed (mm s <sup>-1</sup> )
Larval zebrafish	3.5	0.2	30.0	10.0
	3.5	0.3	54.7	103.8
<b>i</b>	Length (cm)	Ampl. (L)	Freq. (Hz)	Speed (cm s <sup>-1</sup> )
Mayfly larvae	0.98	0.26	26.9	20.8

**Table S1: Kinematic swimming parameters of various swimmers.** **a** Several species of sharks, by Webb et al. [48]. **b** Data reported by Horner et al. [50] on African lungfish. **c** Data reported by Fish et al. [52] for seals. **d** Data reported by Goldbogen et al. [54] for fin whale. **e** Data reported by Sato et al. [57] and by Clark et al. [58] for penguins. **f** Data reported by Muller et al. [40] for larval zebrafish. **g** Data reported by McHenry et al. [62, 63] for Ascidian larvae and *Aplidium constellatum*. **h** Data reported by Budick et al. [64] for larval zebrafish. **i** Data reported by Brackenbury et al. [65] for mayfly larvae.